University of Zurich^{UZH}

Detection of Grounded Ice in Subarctic Lakes using Sentinel-1 Backscatter Time Series

GEO 511 Master's Thesis

Author
Emanuel Vogel
13-925-300

Supervised by
Dr. David Small

Faculty representative
Prof. Dr. Alexander Damm

29.01.2021
Department of Geography, University of Zurich

GEO 511
Master Thesis
January 29, 2021

Detection of Grounded Ice in Subarctic Lakes using Sentinel-1 Backscatter Time Series

Emanuel VOGEL
13-925-300

Supervised by:
Dr. David SMALL

Faculty representative:
Prof. Dr. Alexander DAMM

Remote Sensing Laboratories
Department of Geography
University of Zurich

Abstract

Methane bubbling up from subarctic lakes is one of the contributing factors to climate change. The annual freezing of these lakes influences the methane release, especially the grounding of the ice cover strongly reduces methane emissions. Using Google Earth Engine (GEE) as the primary data source and geospatial computing platform, we investigated and compared grounded ice formation in Barrow, Alaska (USA) and Kytalyk, Yakutia (Russia) from 2017 to 2020. Using Sentinel-1 SAR data, we took into account all four polarisations (HH, VV, HV and VH). Based on the VV-polarised backscatter time series (12-days revisit intervals), the approximate dates for the annual ice maxima were determined for both study sites. The backscatter frequency distributions of masked lake ice surfaces were then used to set a global threshold value for each polarisation. We found that cross-pol (VH, HV) images individually are not well suited for grounded ice detection, as their thresholds need to be set too close to the Noise Equivalence Sigma Zero (NESZ) noise floor to produce plausible results. The co-polarised classifications on the other hand, produced results at both study sites that were in agreement with Joint Research Center (JRC) ERA5 climate reanalysis weather data. From 2017 to 2019, both study sites showed a steady increase in grounded ice of around +3% in Barrow and +6% in Kytalyk. In 2020, the grounded ice percentage in Barrow strongly rose (+9%) from 2019, while in Kytalyk, less grounded ice was formed (-3%). The detected grounded ice fractions were much higher in Barrow (between 32 and 48%) than in Kytalyk (5 - 14%), indicating deeper lakes in Kytalyk. The co-pol map products were very similar to each other, with overall consistencies always staying above 90% in all tests conducted. However, VV-based classifications always detected more grounded ice (between +0.38 and +4.33%) compared to the HH-classifications. We found that these deviations are positively correlated with the relative grounded ice area detected on site. By either multiplying (HH) or dividing (VV) grounded ice fractions by 0.9, the percentages detected by the other co-pol-based classification could always be approximated (±0.24%). A separate consistency assessment of our HH-pol classification method with a dataset by Duguay and Wang (2018) yielded overall consistencies of over 97%, with most errors originating from a slight overestimation of grounded ice.

Contents

Abbreviations

ASTER	Advanced Spaceborne Thermal Emission and Reflection Radiometer
DEM	Digital Elevation Model
ECMWF	European Centre for Medium-Range Weather Forecasts
ESA	European Space Agency
EW	Extra-Wide Swath (Sentinel-1 acquisition mode)
GEE	Google Earth Engine
GRD	Ground Range Detected
GRDH	GRD high resolution
GRDM	GRD medium resolution
GSD	Ground Sample Distance
GTC	Geometrically Terrain Corrected
IW	Interferometric Wide Swath (Sentinel-1 acquisition mode)
JAXA	Japan Aerospace Exploration Agency
JRC	Joint Research Centre
LaSRC	Land Surface Reflectance Code
LST	Land Surface Temperature
MODIS	Moderate Resolution Imaging Spectroradiometer
NASA	National Aeronautics and Space Administration
NESZ	Noise Equivalence Sigma Zero
OLI	Operational Land Imager
RTC	Radiometrically Terrain Corrected
S1	Sentinel-1
SAR	Synthetic Aperture Radar
SM	Strip Map (Sentinel-1 acquisition mode)
SR	Surface Reflectance
SRTM	Shuttle Radar Topography Mission
TM	Thematic Mapper
USGS	United States Geological Survey
WV	Wave (Sentinel-1 acquisition mode)

List of Figures

List of Tables

1 Introduction

The energy exchanges between the atmosphere, water-bodies, and land surfaces are highly complex. Particularly in the Arctic cryosphere, where the seasonal thawing of the former continuous permafrost modifies the landscape and leads to the formation of thermokarst lakes (Kokelj and Jorgenson, 2013). These lakes, that are most commonly found in northern Alaska, Canada and Siberia, are not only indicators of climate change but also contribute to it, as they are sources methane, bubbling up from pleistocene sediments on their beds, (Walter et al., 2007). CO_2 exchange between the atmosphere and the permafrost soil is another component that can be influenced by the freezing of subarctic lakes. Whether these lakes are net sources or sinks of CO_2 is subject of ongoing research (Olivas et al., 2010; Zona et al., 2012; Anthony et al., 2014). During the winter season, thermokarst lakes usually completely freeze over. Because of their shallowness and the surrounding icy air temperatures, the ice cover can often grow thick enough to freeze onto the lake bed. This ice is then known as *grounded ice* or *bedfast ice*. While floating ice does impede the CO_2 exchange with the atmosphere, it does not prevent the methane from escaping through pores in the ice. However, in the case of the ice grounding to the lake bed, this flux is retained because the top layer of the sediments freezes as well (Zimov, 1997). As both, CO_2 and methane are powerful greenhouse gases, monitoring the freezing of these lakes and estimating the proportion of grounded to floating ice is important to improve our understanding of the climatic feedback related to global warming (Muster et al., 2017).

Due to their remote locations and the freezing temperatures, monitoring thermokarst lakes on site during winter months is nearly impossible and therefore research on grounded ice formation relies heavily on remote sensing. Space-borne Synthetic Aperture Radar (SAR) is the most suitable tool for monitoring grounded ice, as it neither relies on the light of the sun, allowing it to acquire images during the dark arctic winters, nor is it weather dependent, which enables the construction of consistent backscatter time series. Furthermore, due to the ability to easily penetrate ice, SAR has proven to be particularly useful for detecting whether lake ice covers reach the lake-bed or not. The combined scattering effects of the high dielectric contrast of the water-to-ice transition and the vertically oriented tubular bubbles entrapped in the ice, cause floating ice (once it has reached a certain thickness) to act as a corner reflector. This results in frozen lakes to appear very bright in SAR backscatter images. When the ice freezes to the lake-bed however, the radar pulses are only reflected downwards on vertically oriented bubbles as the horizontal water surface has disappeared. Because of this, the microwaves get absorbed by the soil under the ice, resulting in very low backscatter (Wakabayashi et al., 1993). This drop from high to low backscatter associated with the grounding of lake ice was first described and explained by Jeffries et al. (1993) using VV polarised ERS-1 C-band (microwaves) SAR backscatter time series in Barrow, Alaska. Many studies have shown that this characteristic backscatter can also be observed with HH polarised images (Duguay et al., 2002), as well as with sensors operating with different wavelengths such as the L-band (radio waves), Japan Aerospace Exploration Agency (JAXA)-run ALOS satellite (Wakabayashi and Nishito, 2015) and the X-band (infrared), German operated TerraSAR-X (Jones et al., 2013). However according to Engram et al. (2013), X- and C-band SAR are preferable over L-band as they show greater contrast between the two classes. Until now, most of the studies on grounded ice have focused on sites in northern Alaska and Canada (Arp et al., 2011; Surdu et al., 2014; Surdu et al., 2016), and only very few have tackled one of the numerous thermokarst regions located in Russia.

In recent years, the quality and availability of space-borne SAR data has improved. It used to be (and still is) the norm that images from most SAR satellite constellations are either accessible only in certain countries for certain institutions and/or are locked behind a paywall. But recently, there has been a trend towards making more earth observation satellite data (including SAR) freely accessible (Loveland and Dwyer, 2012; Wulder et al., 2012; *International Cooperation Copernicus* 2021). European Space Agency's (ESA) Sentinel-1 (C-band SAR) constellation is exemplary for this. Sentinel-1 consists of 2 satellites (Sentinel-1A and 1B), which enables the creation of time series with temporal resolutions over a given position of up to 6 days (Potin et al., 2016). This makes Sentinel-1 a highly attractive option for grounded ice mapping, especially considering the free access to its products. And with Sentinel-1C and 1D already underway to replace them in time, the seamless future expandability of studies is secured (Torres et al., 2017). This is very fortunate for time series analysis, as consistent perspective (flight path), acquisition mode and sensor calibration are very important for comparability. Sentinel-1 is a relatively recent satellite constellation (launched in 2014 and 2016) and up until now, only very few studies on grounded ice had had the opportunity to use it for grounded ice detection (Duguay and Wang, 2019). Unlike most older SAR sensors, Sentinel-1 is able to send both vertically (V) as well as horizontally (H) polarised pulses and usually always receives in both polarisation (HH+HV, VV+VH) which opens up new possibilities for many applications.

Geospatial analysis on large, high resolution satellite imagery is notorious for either testing the patience of the user waiting for the calculations to finish or requiring expensive workstations with high computational power. Google Earth Engine (GEE) is a cloud-based platform that is especially designed for large scale analysis of satellite imagery. It not only offers an integrated programming platform linked to a high-performance computing system but also grants direct and simple access to freely available satellite imagery and their derived products. GEE therefore opens up the field of geospatial analysis to a wider audience apart from traditional, academic science (Gorelick et al., 2017). Grounded ice detection and mapping using SAR time series is a task that involves large amount of data and non-negligible computation power. Because of this, GEE is an attractive tool for this purpose. However, to our knowledge, no studies on ice regime classification have yet been conducted on the platform.

In this study we created annual grounded ice classification maps in GEE using Sentinel-1 data to asses how suitable the Sentinel-1 sensor as well as the GEE platform is for grounded ice mapping. We put special efforts into analysing and comparing all four polarisation modes concerning their suitability for grounded ice mapping, something which to our knowledge has never been done before. Additional focus was put on the correlation between grounded ice formation and climate indicators in a similar fashion to how it was previously done by Surdu et al. (2014). Also, we used relatively simple data analysis and thresholding methods and restricted ourselves to data which were freely accessible directly in GEE (with one exception of one dataset, see Section 3.6). This was done because it was our aim to devise a lake ice classification method that could be implemented on any thermokarst region with minimal equipment and expertise in order to accelerate the quantity of data generated in this field to further advance understanding of the climate system. As primary study sites, we chose two different locations: Barrow (USA) and Kytalyk (Russia). Barrow was chosen due to many studies already conducted in this region (Jeffries et al., 1993; Engram et al., 2013; Surdu et al., 2014), giving us the advantage of already knowing beforehand, what magnitudes of ice proportions we could expect. Kytalyk on the other hand was chosen because in 2018, we had already worked on a small scale study on grounded ice in Kytalyk with two fellow students, expecting to find similar ice regimes as in Barrow. Surprisingly however, we were unable to detect any grounded ice there (see Appendix). In a recent study, Duguay and Wang (2019) nevertheless managed to find grounded ice in Kytalyk. With this work, we therefore intended to follow up on that study and find out why our previous *Quest for Grounded Ice* had failed. While doing this, we also proceeded to answer the following research questions:

1. How well can we map grounded ice in Barrow and Kytalyk with Sentinel-1 and other data freely accessible in GEE?
2. How well do different polarisations work for classifying lake ice?
3. How well can we detect temporal changes in grounded ice formation between 2017 and 2020?
4. What are differences in grounded ice formation between Kytalyk and Barrow?

2 Study areas

2.1 Primary Study Sites

2.1.1 Barrow, Alaska (USA)

This region is named after the City of Utqiaġvik, also known as Barrow (officially until 2016), which is located at the northernmost tip of the US State of Alaska. The landscape around here is characterised by an abundance of shallow thermokarst lakes formed by partial melting of the permafrost soil. The study site is around 3000 km^2 in size, and located between Utqiaġvik in the north and the city of Atqasuk in the south. Most of the lakes are relatively small, but their surface areas can get up to around 33 km^2 in size. Avarage daily temperatures in summer can reach up to 9°C, while in winter, they often drop beneath -28°C.

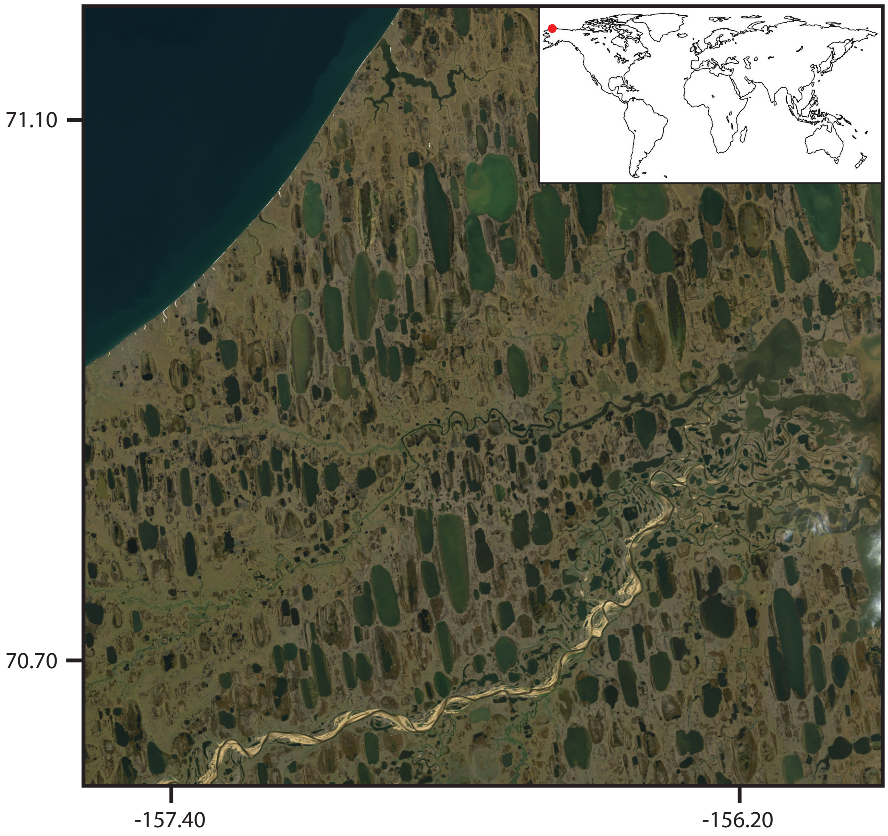

FIGURE 2.1: The Region of Kytalyk captured by Landsat 8 on 11.07.2019 (WGS 84, EPSG:32605).

2.1.2 Kytalyk, Yakutia (Russia)

Kytalyk is located in the north-east of the Russian Republic of Sakha (Yakutia) and encompasses the area around the northernmost part of the *Indigirka* river (regionally called *Protoka Ularovskaya*). Like Barrow, it is a sub-arctic thermokarst region with hundreds of lakes. Parts of the region around the river *Indigirka* and its smaller feeders are subjects to large seasonal and inter-annual changes due to frequent flooding events, while other parts are more static throughout the decades. We therefore mainly focused on these more stable areas in the northwest of the *Indigirka* river valley as the need to consider flooding event could complicate the interpretation of the SAR data. Our site of interest is about 18000 km^2 in size, with several lakes reaching sizes of up to 100 km^2. In Kytalyk, temperatures are even more extreme than in Barrow, frequently surpassing 16°C in summer, while the winters are freezing, with average low temperatures of -37°C. Many studies have been conducted in this area about hydrological, biological and biochemical processes (Klerk et al., 2014; Siewert et al., 2014; Teltewskoi et al., 2016).

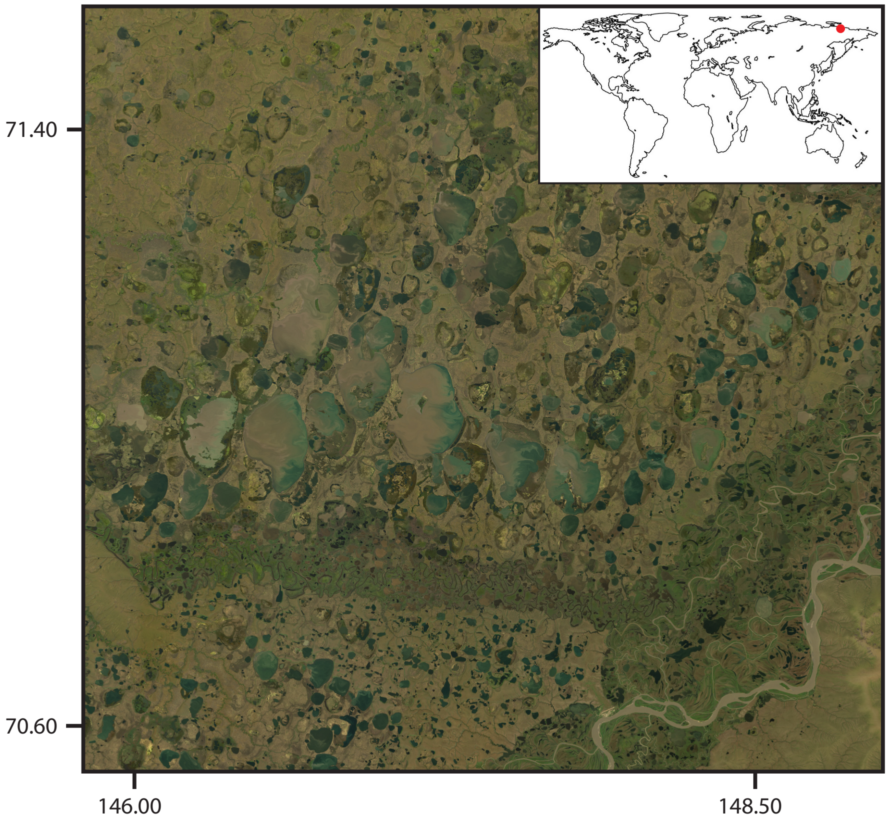

FIGURE 2.2: The Region of Kytalyk captured by Landsat 8 on 13.08.2018 (WGS84, EPSG:32655).

2.2 Secondary Study Site - Churchill, Manitoba (Canada)

The lakes southeast of the small town of Christchurch, located in the northern parts of the Canadian province of Manitoba at the shore of the Hudson Bay, are our last objects of interest. In contrast to both Kytalyk and Barrow which are located far north of the Arctic Circle, these lakes lie around 58.7°N. The temperatures, however, are lower here than in other places of similar latitude, due to the lack of influence of a warm stream. Because of this, the average daily temperatures in the winters are usually far below -20°C. Therefore, the lakes here freeze like in subarctic regions further north. Here we look at lakes scattered over a much smaller area compared to the other sites of around 60 km^2. Since Churchill has both an airport as well as a railway connection to the rest of the north American continent, this location is comparatively easily accessible to perform *in situ* measurements such as done by Duguay and Lafleur (2003).

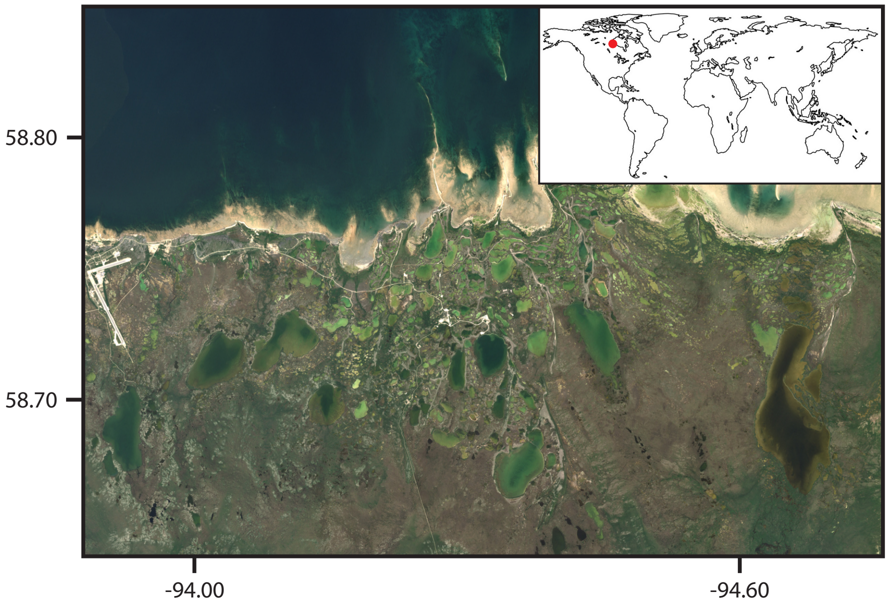

FIGURE 2.3: The Churchill lakes captured by Sentinel-2 on 30.07.2019 (WGS84, EPSG:32515).

3 Data

3.1 Data access and analysis - Google Earth Engine

The Google Earth Engine (GEE) is a free cloud computing platform developed for analysis and visualisation of satellite imagery and geospatial datasets. GEE grants fast access to data by offering a large catalog (`developers.google.com/earth-engine/datasets/catalog/`) of satellite imagery, geophysical and weather/climate datasets, all already geocoded (WGS84 by default) and preprocessed (Gorelick et al., 2017). All data used in this study was accessed and analysed directly in GEE with the exception of a bedfast ice mapping dataset compiled by Duguay and Wang (2018) (for details on that, see Section 3.6). That dataset was acquired separately and then loaded into GEE for analysis.

3.2 SAR Data - Sentinel-1

Sentinel-1 is a SAR satellite constellation where each satellite has a C-Band (5.4 GHz centre frequency) sensor on board. The satellites are part of the ESA Copernicus Programme. Currently there are two Sentinel-1 satellites: Sentinel-1A launched in April 2014 and Sentinel-1B in April 2016. Depending on whether both or only one of the two satellites acquire data over a given position is determined by the current observation scenario - this implies an exact repeat interval (on the same orbit) of either 6 or 12 days (Potin et al., 2016). The satellites are able to operate in 4 different acquisition modes depending on the observation target: Strip Map (SM), Interferometric Wide Swath (IW), Extra-Wide Swath(EW) and Wave (WV). EW is usually used while the sensor is over the ocean while IW is the standard acquisition mode over land. SM and WV are not further relevant in this work and are also not available in GEE. They therefore are not further reviewed here. The Ground Range Detected products (GRD) of the IW, and EW modes can have a Ground Sampling Distance (GSD) of up to 10 m (IW) or 25 m (EW) respectively. Due to the different swath widths of the modes, incident angles change as well (see Table 3.1), which should be considered when comparing backscatter values of images covering the same location acquired with the same sensor using different imaging modes.

TABLE 3.1: Overview of Sentinel-1 acquisition modes available in GEE

Acquisition Mode	Reference	Ground Sample Distance	Swath Width	Incident Angle Range
interferometric wideswath	IW	10 m	250 km	29 - 46°
extra wideswath	EW	25 m	400 km	19 - 47°

The satellites can operate in either single or dual polarisaton modes: In polar regions, images are typically acquired in EW with HH or HH+HV polarisations, while otherwise over land IW mode with VV or VV+VH polarisations is employed (Potin et al., 2012; Potin et al., 2019). Note however that the above described products are not always available in their full resolution in the GEE, and polarisation modes could have changed over time due to adjustments in the Observation Scenario. A thorough inspection of the available data for a given time frame and location is therefore always necessary. Sentinel-1 images are always input to the GEE from GRD products using the ESA SNAP software tool. Thermal noise is removed, with radiometric calibration to backscatter coefficient σ^0 in dB using GRD metadata as well as orthorectified using NASA's Shuttle Radar Topography Mission (SRTM) 30 meter Digital Elevation Model (DEM) or the Advanced Spaceborne Thermal Emission and Reflection Radiometer (ASTER) DEM for latitudes over 60°. All pre-processing steps (see Figure 3.1) were performed by Google using the Sentinel-1 Toolbox component (S1TBX) of the ESA SNAP software (Zühlke et al., 2015; Filipponi, 2019).

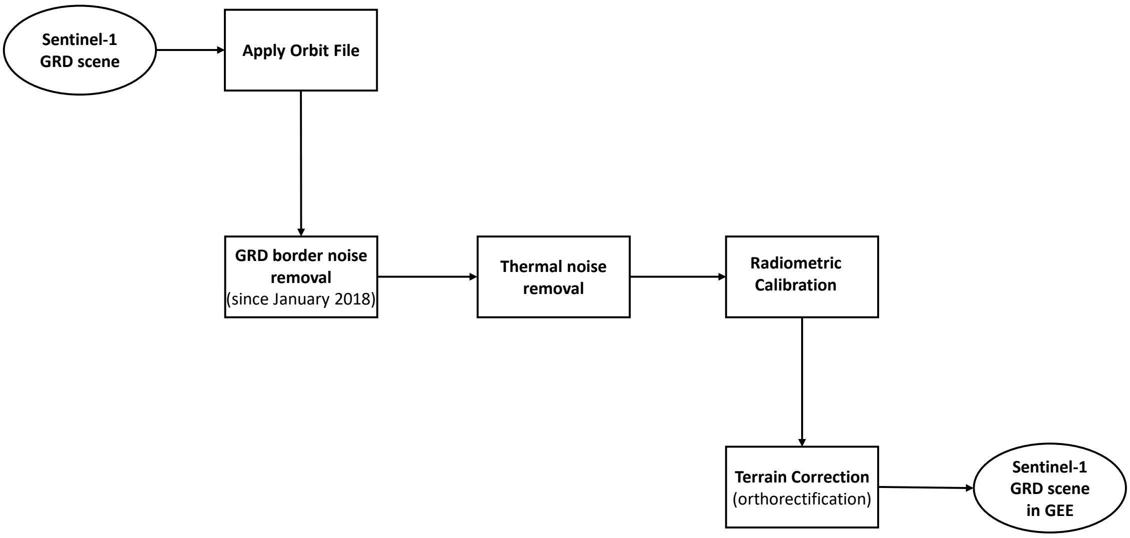

FIGURE 3.1: The pre-processing steps applied to Sentinel-1 GRD products at the input stage to GEE using the SNAP S1TBX.

3.3 JRC Global Surface Water

The Global Surface Water dataset produced by the Joint Research Centre (JRC) of the European Commission shows where and when water bodies were present between 1984 and 2019 at a global scale. The dataset was created from images acquired from NASA's Landsat 5, 7 and 8 Satellites using the spectral properties of water across the visible, near and shortwave infrared bands to identify and map the water bodies for each Landsat scene that passed the quality test. The results were combined into a monthly history for the entire time period (1984 to 2019) for change detection. The resulting global scenes have a spatial resolution of 30 m originating from the GSD of Landsat (Pekel et al., 2016). There are also multiple derivates of this data collection available on

GEE apart from the original monthly history. In this work, we used the yearly aggregation of the monthly classification, denominated: JRC Yearly Classification History, v1.2.

3.4 Optical Data

3.4.1 Landsat 8 OLI

Landsat 8 is an earth observation satellite and the most recent addition (launched in February 2013) to the well-known Landsat program run by the National Aeronautics and Space Administration (NASA) in collaboration with the United States Geological Survey (USGS). Its Operational Land Imager instrument (OLI) is a push-broom Sensor operating at wavelengths ranging from 0.43 to 2.30 µm partitioned into 9 spectral bands, thus covering the visible, near infrared and short wave infrared spectral range. Operational since May 2013, it takes images of the Earth's land surface with a GSD of 30 m and a swath width of 185 km, repeating its track every 16 days (Knight and Kvaran, 2014). The Landsat 8 images on GEE are available in multiple variations of applied processing steps and tier levels, but in this thesis, we only used tier 1 (highest quality) surface reflectance images. The processing to surface reflectance was done with the Land Surface Reflectance Code (LaSRC) (Vermote et al., 2018; Feng et al., 2012).

3.4.2 Sentinel-2 MSI

Sentinel-2 is, like Sentinel-1, part of ESA and the EU's Copernicus Programme. It is a constellation consisting of two satellites: Sentinel-2A and -2B, launched in June 2015 and March 2017 respectively. They are equipped with the Multispectral Instrument (MSI) which measures Earth-reflected sunlight at wavelengths ranging from 0.44 to 2.19 µm in 13 bands, resulting in higher spectral resolution overall compared to OLI at the expense of bandwidth. The GSD of MSI data ranges from 10 to 60 m with the 3 visible and the near-infrared bands having the highest spatial resolution, i.e. 3 times that of OLI in these spectra. The interval between repeat tracks is 5 days , with more frequent revisit possible due to the overlap resulting from the 290 km swath width at higher latitudes. Unlike OLI however, MSI is turned off over the ocean (Drusch et al., 2012). In GEE, MSI Data is offered both as top of atmosphere reflectance (Level-1C) as well as SR (Level-2A). For this thesis, we only considered images categorised as Level-2A (Louis et al., 2016).

3.5 Climate Data

3.5.1 MODIS LST

The Land Surface Temperature (LST) dataset used in this work is a derived product of the Moderate Resolution Imaging Spectroradiometer (MODIS) instrument installed on the two NASA satellites Terra and Aqua (launched in 1999 and 2002), formerly known as EOS-AM1 and EOS-PM1. MODIS has a total of 36 spectral bands, within a spectral range from 0.4 to 14.4 µm. In exchange for this considerable spectral resolution and bandwidth, it has a GSD of 1 km but a swath width of 2,330 km, which allows for time series with high temporal resolution. The LST product is derived from the thermal infrared bands 31 and 32 using a special algorithm that takes into account land cover types as well as atmospheric water vapour (among other atmospheric effects) to estimate thermal land emissivity and therefore temperature at ground level (Wan et al., 2004). Due to the limitation of passive spaceborne remote sensing systems such as MODIS of not being able to see through clouds, the accuracy of these estimations are heavily dependent on weather (Wan, 2008). The resulting dataset with global coverage is made freely available both at daily and 8-Day aggregate levels in GEE.

3.5.2 ECMWF ERA5

ERA5 is a climate reanalysis dataset based on model calculations produced by the Copernicus Climate Change Service of the European Centre for Medium-Range Weather Forecasts (ECMWF). The product is produced with the goal of creating a global record of atmospheric, land and oceanic climate by combining physical model calculations with observation data. The dataset has a spatial sample interval of 31 km, and is made available as daily and monthly aggregates while the reanalysis itself is calculated on an hourly basis. Although it has a much lower spatial resolution than MODIS LST, it contains additional information beyond mean, minimum and maximum temperature, such as wind intensity and direction, precipitation and air pressure. Because ERA5 combines multiple methods and data sources into one product, the accuracy of the data is temporally more consistent compared to other products such as LST (Hersbach et al., 2020). In GEE, the ERA5 data is available as daily and monthly aggregates. In this work we solely used the daily aggregate products.

3.6 Lake Ice Classification by Duguay and Wang (2018)

In 2018, Duguay and Wang published a dataset with the title: *Lake Ice Classification from Sentinel-1A 2015 - 2018*, where they distinguish grounded from floating ice for 8 different subarctic study sites, including our primary study sites Katalyk and Barrow, using Sentinel-1 EW HH-polarised data. They used 3 different methods for each site to map bedfast lake ice: threshold, K-means and an Iterative Region Growing algorithm. In this thesis, we are mainly interested in their classification using the threshold algorithm, as this comes closest to the methods applied in this thesis. They assessed Duguay and Wang (2019) this methodology to provide the highest accuracy (92.56%) of the 3 methods. For Barrow, the dataset includes classifications for April 2015, 2016 and 2017) while for Kytalyk, only data for April 2015 and 2016 was provided.

4 Methods

4.1 Sentinel-1 data coverage over study sites

As alluded to in the previous chapter (Section 3.2), the Sentinel-1 data acquisition mode as well as the associated polarisations often change at the transition from the arctic sea to the landscapes of northern Alaska and northern Yakutia respectively. While this presents us with a challenging data situation as these border-regions were for some time especially susceptible to changes in the observation scenario by ESA, it is also a rare chance, since we have an overlapping area of HH+HV and VV+VH polarised images. The benefit of this data analysis is therefore not only to identify the revisit period of the satellites and hence to identify the time span where we have adequate data to construct a time series, but also to delineate the areas of this overlap of acquisition modes within the larger confines of our two primary study sites. To do this, we we used the filter functions in GEE on the Sentinel-1 image collection, so it would pre-select images of our study sites. We restricted ourselves to using only images from descending orbits to ensure comparability between Barrow and Kytalyk, given that Barrow is covered also during ascending orbits, while Kytalyk is not. From here, we could then narrow the data down to the most suitable relative orbits for our time series and polarisation analyses.

For Barrow, there were three orbits available covering a sizeable overlapping area within the region (see Figure 4.1). Two of the orbits acquired in IW mode (VV+VH polarisations), are suitable for constructing continuous time series, as they have a revisit frequency of 12 days and only very few gaps in coverage between 2017 and 2020. The gaps mainly fell outside of our main months of interest (November - May). It must be noted though, that for both IW/44 (Aq. Mode/Relative Orbit Number) and IW/73 we are limited to using VV polarisation only if we want to cover all 4 years, as Sentinel-1 only used single-VV polarisation mode up until mid-2017 over this region. The EW/117 was only available in GEE based on GRDM (GRD medium resolution) of 40m, with just enough data for 2017, 2019 and 2020 around April, which is when we usually expect the lake freezing to reach its maximum, and to be able to make clear comparisons between VV and HH polarisation threshold classifications for those 3 years. While both IW/73 and EW/117 cover the full area of the Duguay and Wang (2018) dataset from April 2017, IW/44 goes only up to cover about two thirds of it - this lead us to restrict our study site to an area of nearly 1530 km^2 (see Figure 4.2).

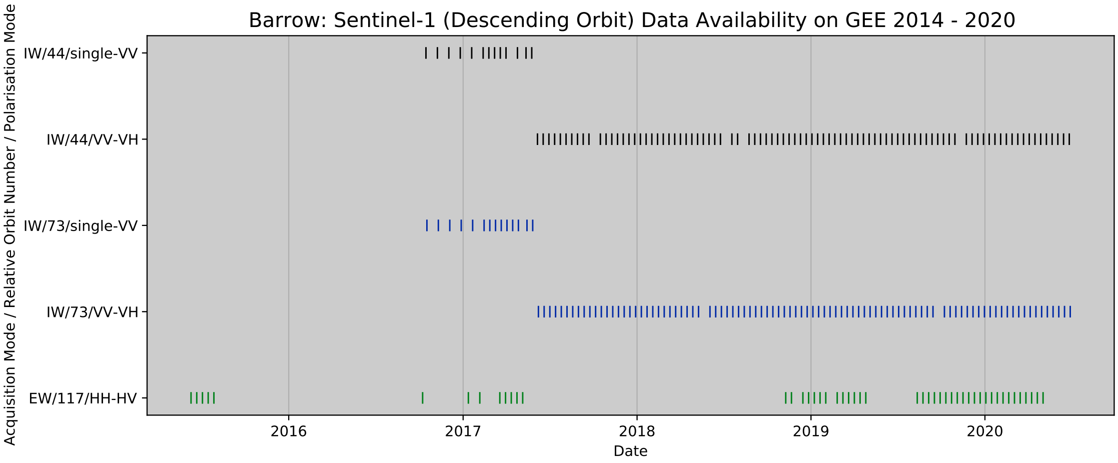

FIGURE 4.1: Each tick represents a Sentinel-1 product covering the Barrow lakes in GEE up to June 30, 2020.

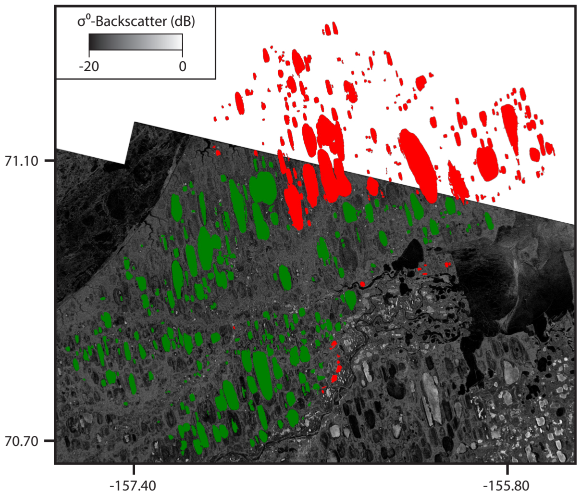

FIGURE 4.2: IW/44 (EPSG:32404) acquisition pattern narrows down study area in Barrow to the southern half compared to the lakes covered by Duguay and Wang (2018) (all marked lakes). The lakes in green are in our dataset, while the lakes in red were cut.

Looking at the second primary study site Kytalyk, two relative orbits were suitable for our purposes (see Figure 4.3): IW/90 for constructing time series and EW/163 (again only in GRDM with 40m GSD) to compare polarisations. Within these two relatives orbits, we are much less restricted in comparison to Barrow: IW/90 had full double VV+VH coverage from 2017 to 2020 with only two gaps in its 12 days repeat interval and EW/163 had HH+HV images around all four ice peak seasons from 2017 to 2020. As already mentioned in Section 3.6, Duguay and Wang's dataset covered the peak season dates only from 2015 and 2016 - these 2 years lie outside the 4 year time frame covered by IW/90, so an accuracy assessment for Kytalyk was not possible using data within our primary period of investigation. That being said, GEE did provide access to EW/163 GRDM images covering the peak season of 2016, enabling us to make some comparisons with our own classification method, though not as extensively as in Barrow. Just as in Barrow however, one is again forced to restrict the study site to a smaller area compared to Duguay and Wang, as EW/163 has not covered the whole of the site anymore since March 2017. Before that date, the EW swath on this relative orbit extended further south. Additionally, we also removed part of the area in the southeast, as these lakes are very close to the *Indigirka* river, and are therefore more prone to shoreline changes caused by flooding events. However, there are still many smaller rivers within this region. With an area of over 8400 km^2, this study area is more than 5 times the size of the Barrow site.

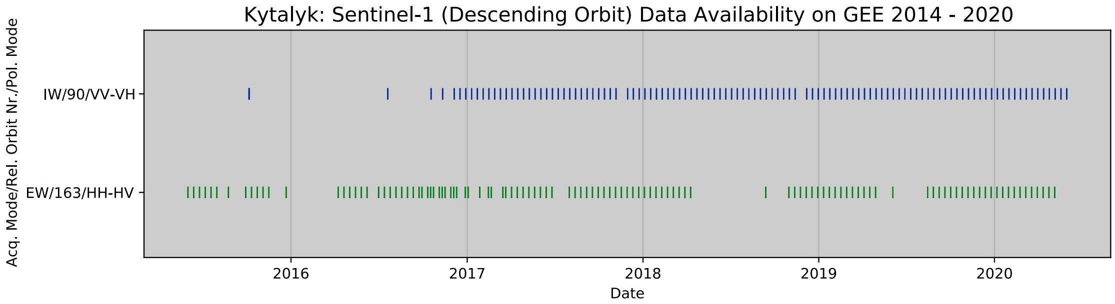

FIGURE 4.3: Each tick represents a Sentinel-1 image covering the Kytalyk lakes in GEE up to June 30, 2020.

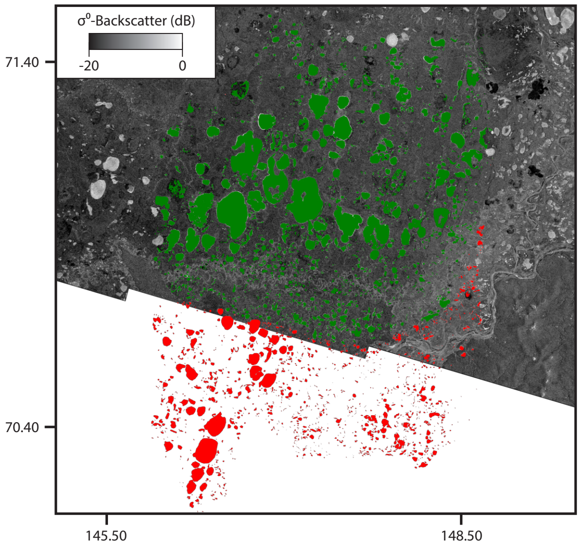

FIGURE 4.4: Since March 2017, the EW/163 (EPSG:32655) acquisition pattern narrowed down our study area in Kytalyk to the northern half compared to the lakes covered by by Duguay and Wang (2018) (all marked lakes). The lakes in green are in our dataset, while the lakes in red were cut.

4.2 Sentinel-1 backscatter re-calibration to γ_E^0

As mentioned in Section 3.2, Sentinel-1 GRD images in GEE were pre-processed to σ^0. As a result of that choice by Google, the backscatter values naturally decrease with increasing viewing incidence angle. This is not ideal in our case, since we prefer to classify relatively large areas using the same backscatter threshold value. Doing this on a σ^0 calibrated image taken from a descending orbit can lead to a systematic classification error in the near to far range direction, since backscatter towards the east is generally higher than towards the west. To eliminate this problem, we recalibrated the σ^0 backscatter values to γ_E^0 using the following equation:

$$\gamma_E^0 = \sigma^0 / cos(\theta_i) \tag{4.1}$$

Since GEE can provide an incident angle θ_i band for each Sentinel-1 scene, we have all information we need for the transformation. θ_i provided by GEE does account for the Earth's curvature, which means that this equation radiometrically corrects backscatter onto the ellipsoid. However, local incident angle deviations caused by sloped ground were ignored. Given that we are observing flat surfaces (lake ice) on topographically very flat regions, these effects are expected to be negligible, or marginal at most. Before we can apply this correction however, we have to convert the logarithmic decibel (dB) backscatter values back to the original, (linear) scale. For this, one can use the formula:

$$linear = 10^{dB/10} \tag{4.2}$$

After the log/linear transformation, we then convert the linear backscatter values again to dB using the definition of dB, as expressed in the following equation:

$$dB = 10 * log_{10}(linear) \tag{4.3}$$

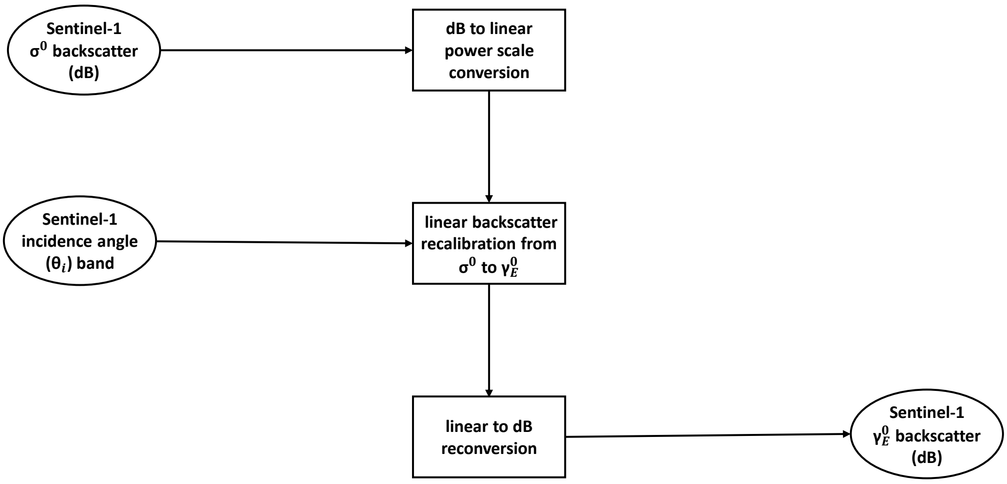

FIGURE 4.5: Flowchart showing the workflow for transforming Sentinel-1 GEE σ^0 to γ_E^0 dB backscatter.

This workflow (see Figure 4.5) was applied to all Sentinel-1 scenes analysed in this thesis.

4.3 Lake mask construction

To isolate the lake ice surfaces from the rest of the image for our backscatter time series analysis, a water mask is needed. Instead of having to construct our own water mask from Landsat or Sentinel-2 images, we can make use of JRC Global Surface Water data (Pekel et al., 2016) for this purpose. As explained in Section 4.1, the data available to us allowed for a time series analysis of the last 4 freezing seasons (2017-2020) at both of our primary study sites. Our intention was to construct water masks for both sites, which are equally valid for all four years, so we have the same area and a similar numbers of pixels for statistical comparability. This means that we intend to solely examine areas where permanent water was observed in all 4 summers previous to our icy seasons. There were a few things we have to consider: as mentioned in Section 3.3, the JRC Global Surface Water datasets were derived from optical Landsat data, and our study sites lie far above the Arctic circle. This means that there is very limited temporal resolution from optical sensors, as they rely on the light of the sun. Cloud cover also limits the number of valid observations. In addition, even during the time period when optical observation is possible, the lakes are often still fully or partially frozen. Using the JRC Global Surface Water Metadata dataset, we can see that during the whole mapping period between 1984 and 2019, there were pixels within both our defined study areas (see Section 4.1, that had less than 40 valid observations over those 35 years. Therefore, visual inspection and subsequent outlier-filtering of obviously unrealistic classifications of the yearly history between 2016 and 2019 was an important step in creating our lake masks. In the case of Barrow, classification from the year 2018 showed quite large diagonal gaps in the permanent water classification, which look like artefacts (see Figure 4.6) and therefore we removed this year from our JRC water collection for Barrow. In the case of Kytalyk, all 4 yearly JRC water classifications seemed to display plausible classifications.

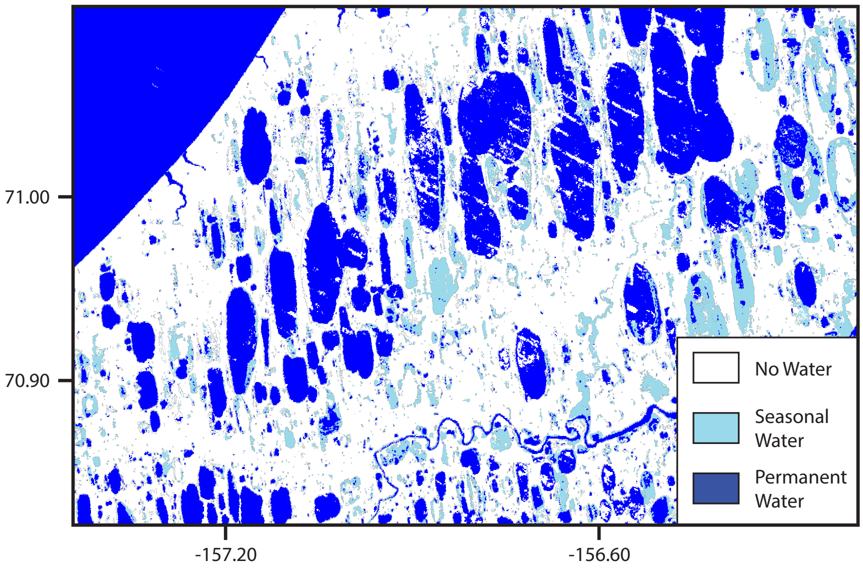

FIGURE 4.6: JRC Yearly Water Classification History 2018 (EPSG:32605). Diagonal lines classified as "no water" interrupt the permanent water class.

After this manual filtering step, we aggregated the remaining classification layers into a single layer containing the pixels that were classified as permanent water over all yearly classifications: 2016, 2017 and 2019 for Barrow and 2016 - 2019 for Kytalyk. Using a pixel counter function, we were also able to remove very small patches of only one or very few pixels in size. The resulting binary images were then used to mask all Sentinel-1 σ^0 backscatter scenes (see Figure 4.7 for the full workflow summary). It is important to emphasise that the primary goal of this method for constructing our lake mask was to make sure that we kept lakes or shorelines that ran dry or conversely water bodies that might have newly formed during our observation period out of the picture to avoid false classifications. This however also meant, that our lake mask tends to rather under- than overestimates our lake areas, which should be kept in mind in the discussion of our results.

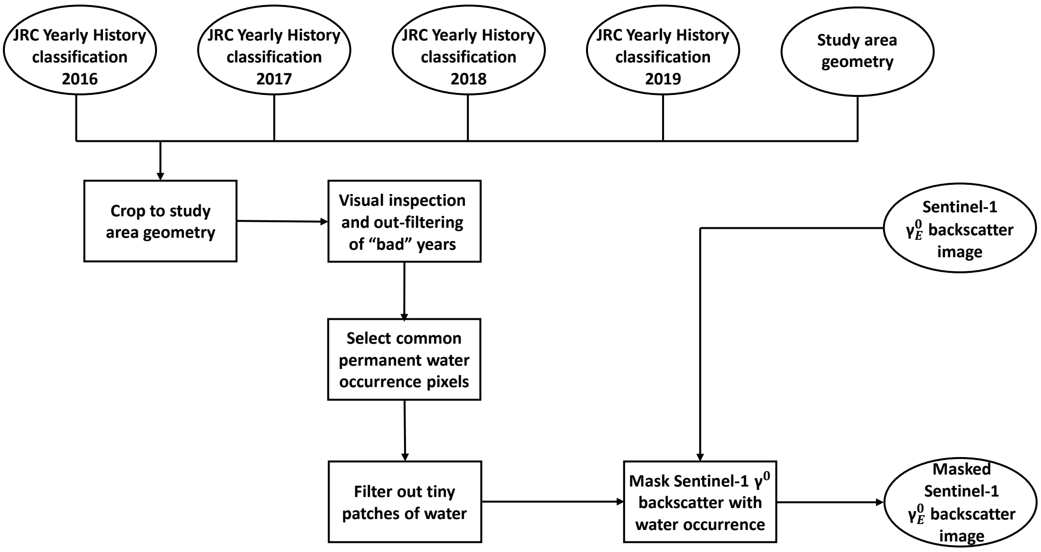

FIGURE 4.7: Flowchart showing the workflow for constructing the lake masks needed to isolate lake ice in the SAR images.

4.4 Determination of seasonal ice maximum

One of the goals of this thesis is to show annual changes in grounded lake ice formation, similar to what has been done for the Barrow area by Surdu et al. (2014) using ERS-1/2 data but without the help of any physically based lake ice models and ground samples. In order to be able to do this, determining the approximate date of maximum ice thickness is very important, as otherwise we could potentially severely underestimate the area of bedfast ice in certain years and therefore distort the magnitude of change between the examined years. The most straightforward way to do this would be to perform the threshold-classification first and then apply it to all SAR scenes acquired from December to May for each year we have available. We would then simply select the scenes with most grounded ice percentage in each year. While this method would be very robust, it is also quite laborious and therefore we opted for a solution that reduced the number of scenes we would have to work with in advance of the actual classification of the ice. It uses the timing and magnitude of the backscatter drops caused by grounded ice observable in lake ice time series as indicative features. During warmer seasons, lake surface SAR backscatter among multiple lakes positioned close to each other is usually very similar, as the lakes are affected by wind and weather in a spatially correlated fashion. But their backscatter can differ greatly in winter, because of the emergence of grounded ice. This difference increases with time through the winter, as long as the temperatures stay freezing cold because more ice freezes onto the lake beds as the ice gets thicker. We can therefore assume that our seasonal ice maximum is where we have the largest difference in backscatter between non-grounding lakes (deep) and the group that includes partially and fully grounding lakes (more shallow).

In order to find these points in time, we first needed to create a consistent SAR time series for both of our study sites. As shown in Section 4.1, IW VV-polarised scenes had the best temporal coverage and also fairly consistent revisit intervals of 12 days at both study sites, making them suitable for this purpose. In GEE, we were able to create an image collection containing all Sentinel-1 IW scenes, acquired from our previously filtered relative orbits (number 44 for Barrow and 90 for Kytalyk). Next, we needed to make a sensible selection of lakes for our time series plot. We had to make sure to include at least one lake per site that did not ground over the whole 4 year period, i.e. it never showed a drop in backscatter until the end of the season, which is usually around mid May to early June. The mean backscatter value of this lake were then our baseline from which we subtracted the average of the (partially) grounded lakes. For the other lakes, we opted for an selection that started to show a drop in backscatter at differing times in the icy season to ensure a representative sample of the variety of lakes. Otherwise we might get a date for the maximum ice extent that is too early, if no lakes were included in the calculation that ground late in the season. We made this manual selection on the basis of masked IW VV γ_E^0 backscatter images from mid April for each year. For all of the selected lakes (see Figure 5.2 and Figure 5.4 in Section 5.1), we then produced a backscatter time series by sorting the mean backscatter of the masked lake surface by the date of acquisition of the images in our collection. The backscatter of the (partially) grounding lake could then be subtracted from the backscatter of the non grounding lake in each image. Finally, we extracted the one IW scene with the highest backscatter difference for each of the 4 years (see Table 4.1 in bold). As we wanted to compare our VV-based ice classifications with other polarisations, in particular HH, we needed to also look for EW scenes acquired on a date as close as possible to our IW selection. For the years 2017, 19 and 20 we have good matches at both study sites with acquisition date differences of around either -1 or +5 days. In 2018 however, there were no EW scenes available in Kytalyk at all (see Figure 4.1 in Section 4.1) and the closest match for Kytalyk was acquired over a month before the corresponding IW scene - this data availability issue needs to be taken into consideration when analysing a classification based on this swath.

TABLE 4.1: Sentinel-1 IW (VV+VH polarised) images (bold) with highest lake surface backscatter difference at both primary study sites from 2017 to 2020. The available EW (HH+HV polarised) scenes with a date of acquisition closest to the corresponding IW scenes are also listed.

	Barrow			Kytalyk		
Ice Season	max. γ_E^0 diff. (dB)	**IW date**	EW date	max. γ_E^0 diff. (dB)	**IW date**	EW date
2017	6.75	***25.04**	24.04	7.19	**10.05**	09.05
2018	7.30	**08.05**	-	8.86	**17.05**	*10.04*
2019	7.99	**21.04**	26.04	11.07	**30.04**	29.04
2020	8.80	**15.04**	20.04	8.96	**24.04**	23.04

* Only VV polarised

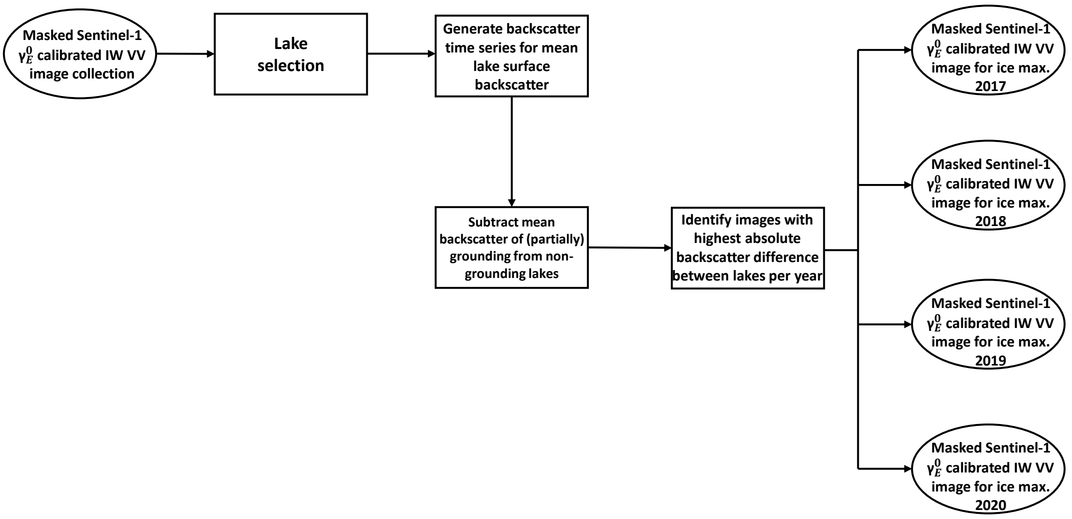

FIGURE 4.8: Flowchart showing the workflow for identifying the date of the maximum lake ice extent (thickness).

4.5 Setting backscatter thresholds for lake ice classification

The next step is to determine the threshold in order to assign the masked γ_E^0 values of our previously filtered Sentinel-1 scenes (see Table 4.1 into one of two groups: floating or grounded ice. As we use two extremely similar C-band sensors (Sentinel-1A and B) for all of our observations, we only need to set one threshold per polarisation mode which should ideally be valid for all images acquired in said mode, regardless of the year of acquisition or study site. To find the correct threshold for each polarisation, we take advantage of the bi-modal frequency distribution of the lake ice pixels. We identify for each polarisation mode the average local frequency minimum over all 4 scenes per study site (or only 3 for VH, HH and HV in Barrow, where there are gaps in our coverage), which we then define as our threshold for all scenes. Unfortunately, not all frequency distributions show such clearly visible approximate double Gaussian curves as in Figure 4.9 (left side). A challenge arises when only a relatively small percentage of the lake ice grounds within an examined region, which is the case in Kytalyk, as we can see in Chapter 5. It means that there are not enough pixels representing grounded ice to form a local maximum in the image histogram, and consequently also no local minimum. The scenes of Kytalyk were therefore not ideal for determining thresholds using this method and we used the thresholds that were derived solely from the Barrow scenes (see Figure 4.9, right side).

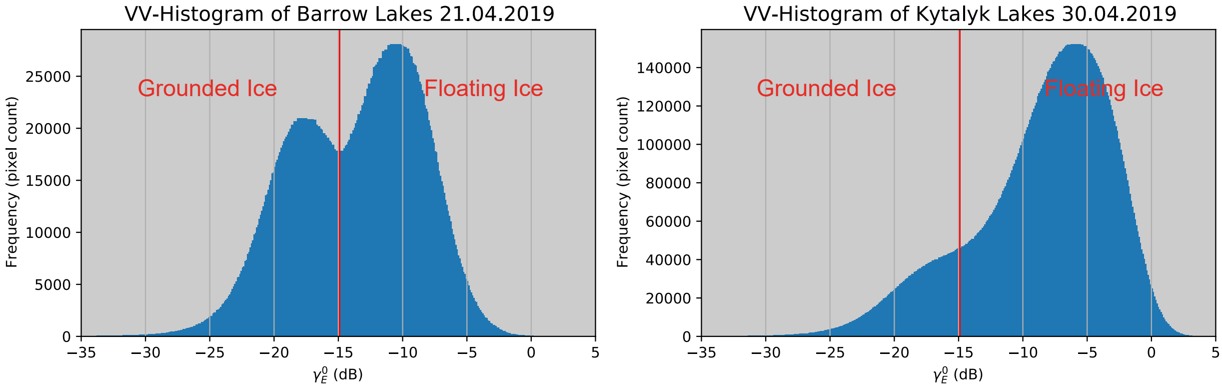

FIGURE 4.9: Frequency distributions of Barrow and Kytalyk lake ice backscatter during state of ice maximum. The bi-modality is much more distinctive in Barrow (left) than in Kytalyk (right). The threshold of 14.9 (red line) was determined based on the local minima of all 4 VV polarised Barrow scenes. Backscatter below the threshold is classified as grounded, backscatter values above the threshhold as floating ice.

A further issue was that VH and HV were problematic, as the two clusters barely showed any separation, which is already a hint concerning their adequacy for mapping grounded ice. The poor separatbility not only gave us low confidence in the determined cross-pol. threshold because the local minimum was barely discernible; it also ultimately resulted in more erroneously classified pixels, as the intersecting area between the two clusters increases. The cross-pol backscatter was typically closer to the sensor's NESZ noise floor (Miranda et al., 2017) - it appeared that changes affecting backscatter values below -25 dB occurred either due to the calibration or the preprocessing of the VH and HV data, making comparisons of the histograms between the individual years more difficult to interpret. Hence we had to base our threshold on only one or two scenes, further lowering our confidence in classifications based on the cross-pol channels (see Table 4.2).

TABLE 4.2: Local minima in the frequency distributions of the Barrow scenes (see Table 4.1) used to determine the γ_E^0 thresholds for the ice classification. All values are reported in dB. Scenes marked as "unclear" were affected by changes in the VH and HV data and were therefore difficult to interpret. The final thresholds were determined as the rounded means of their corresponding yearly minima.

	IW		EW	
	VV	VH	HH	HV
2017	-14.9	-	-12.5	unclear
2018	-15.1	-22.5	-	-
2019	-15.2	-22.9	-12.8	-26.9
2020	-14.4	unclear	-12.9	unclear
Threshold:	**-14.9**	***-22.8***	**-12.7**	***-26.9***

4.6 Preparation for statistical analysis

We could now apply our determined thresholds to our scenes, giving us our final product: A yearly classified time series, showing the ice maximum for each year from 2017 to 2020. But as seen in Section4.1, the EW HH+HV polarised swaths available in GEE were based on GRDM (40m) resolution, while VV+VH polarised IW was available in its native 10m GSD resolution. One of our research questions asked about how well different polarisations work for mapping grounded ice. For statistical comparisons, we needed to bring both datasets into a common resolution. Similarly, for our comparisons with Duguay and Wang (2018), where even three different resolutions were to be compared, a common resolution was defined: their data set was based on an original HH-polarised band which had a 25m GSD. For our data resampling, we adhered to the following three rules:

1. Always resample directly the masked Sentinel-1 γ_E^0 scenes and apply the thresholds we had determined based on their originally available resolution in GEE after the resampling step.

2. If possible, reduce through averaging the resolution of the scene with the higher resolution (IW, 10m) to match the one with the lower (EW, 40m). Exception: when we compared with Duguay and Wang (2018), we opted to match their sample interval of 25m.

3. When we reduce resolution, we take the mean γ_E^0 value of the finely sampled pixels to assign to the new coarser interval. When moving from a coarser sample interval to a finer one, we used bi-linear interpolation.

4.7 Scene selection for accuracy assessment with Duguay and Wang (2018)

The comparison of our lake ice classifications with those reported by Duguay and Wang is an important part of this work as there were no *in situ* measurements available to us of lake depth in both regions to check whether or not our classifications would correspond. While their data set is by no means a replacement for an accuracy assessment using ground truth, given that their classification is not perfect either (92.56% accuracy for the threshold method), it can still provide some important context regarding the validity of our thresholds and the utility of the different polarisation modes for mapping grounded ice.

As mentioned in Section 3.6, the data set contains multiple scenes from 2015 to 2017 for both Barrow and Kytalyk. We therefore needed to select the most suitable scene for each study site. The selection for Barrow was relatively simple, as their dataset contains a classification map from 24.04.2017, which matches exactly the EW scene we identified as the one taken closest to the time of the ice maximum of that year (see Table 4.1). Also, as their classification was based on Sentinel-1 EW scenes, we assume that they used the GRDH (GRD high resolution) version of this exact EW scene (relative orbit 117) for their map. In addition, we have the IW scene from one day later (25.04.2017), giving us the opportunity to test our classifications based on HH, HV and VV. For Kytalyk, we had no choice but to utilise a scene outside of our time series, as Duguay and Wang only included scenes from 2015 and 2016. Here we chose an EW image from 20.04.2016, again perfectly matching one of their maps. Unfortunately there are no IW scenes available in GEE acquired around April 2017 (see Figure 4.3), so we could analyse our classifications based only on HH and HV.

It is important to note that for these comparisons, we used Duguay and Wangs own classification maps, which were beforehand cut to our own defined study areas (see Section 4.1) for masking the Sentinel-1 scenes, in order to have the same coverages. The tested thresholds applied were completely based on our time series utilising our own lake mask (see Section 4.3).

5 Results

5.1 Lake ice backscatter time series (IW VV)

In this section, we visually analysed the backscatter intensity time series of the lakes (see Figure 5.2 and 5.4) we previously selected in order to identify the annual ice maxima. The time series for both study sites (Figure 5.3 and 5.5) covers a time span of more than 3 and a half years, starting in late 2016 and ending in mid 2020. As we have seen in Section 4.1, only VV polarised IW swaths have enough temporal consistency to cover the whole time period. We are therefore unfortunately not able to extend this analysis to other polarisations. In the following paragraph we first focused on the Barrow lakes time series.

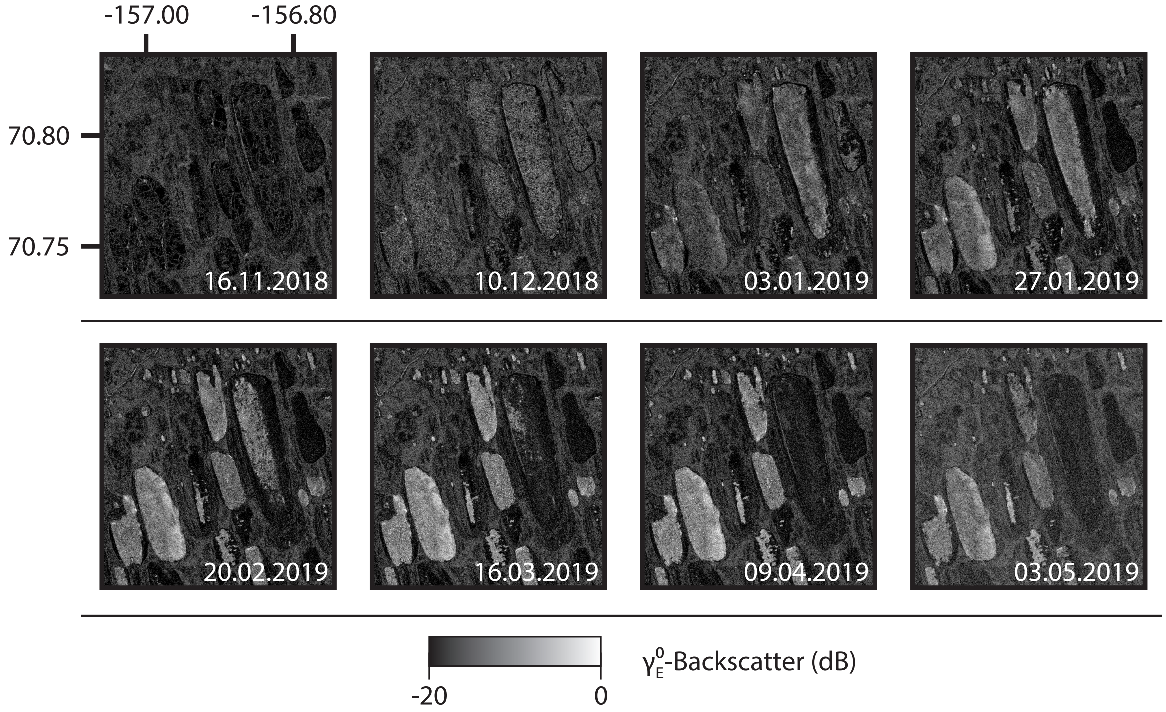

FIGURE 5.1: γ_E^0 VV backscatter image series of Lake 2 and surrounding lakes (24-days interval, EPSG:32604). In the first three images (16.11.2018 to 03.01.2019) the overall backscatter of the lake-surfaces increases as the floating ice covers grow in thickness. From 03.01. to 09.03.2019 the grounded, dark regions at the shallow shores of Lake 2 (largest lake) grows successively inwards, until the whole lake is grounded. Meanwhile, the surrounding (deeper) lakes exhibit further backscatter increase as the floating ice thickens further.

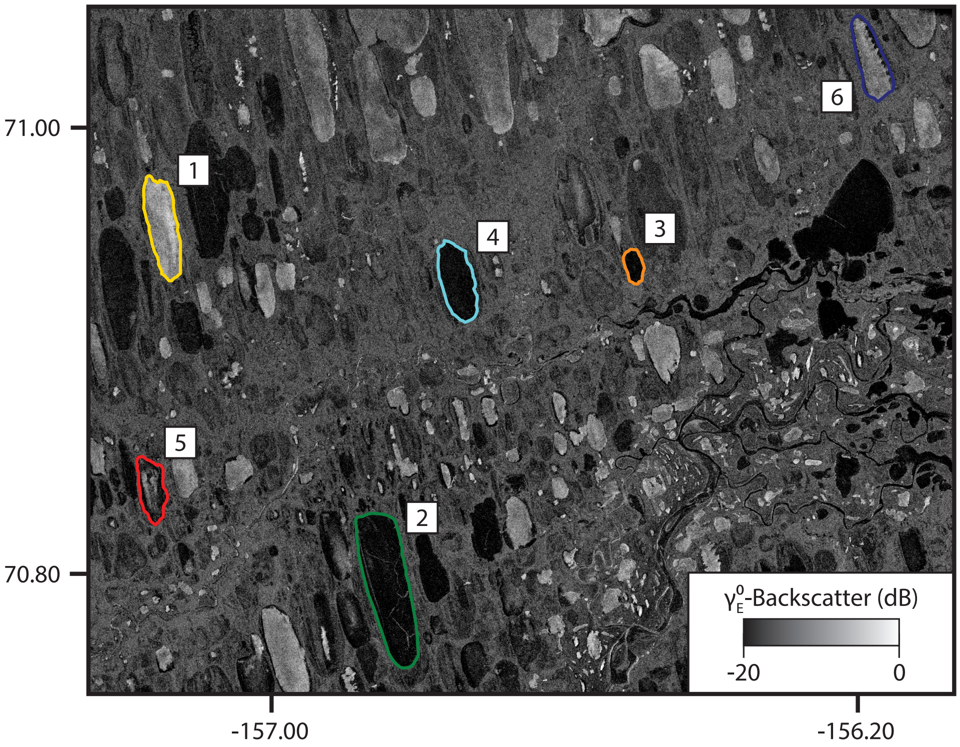

FIGURE 5.2: Barrow: IW VV polarised γ_E^0 backscatter image from 15.04.2020 (EPSG:32504) with marked selection of lakes (1-6) used for the determination of the annual ice maximum (see Section 4.4).

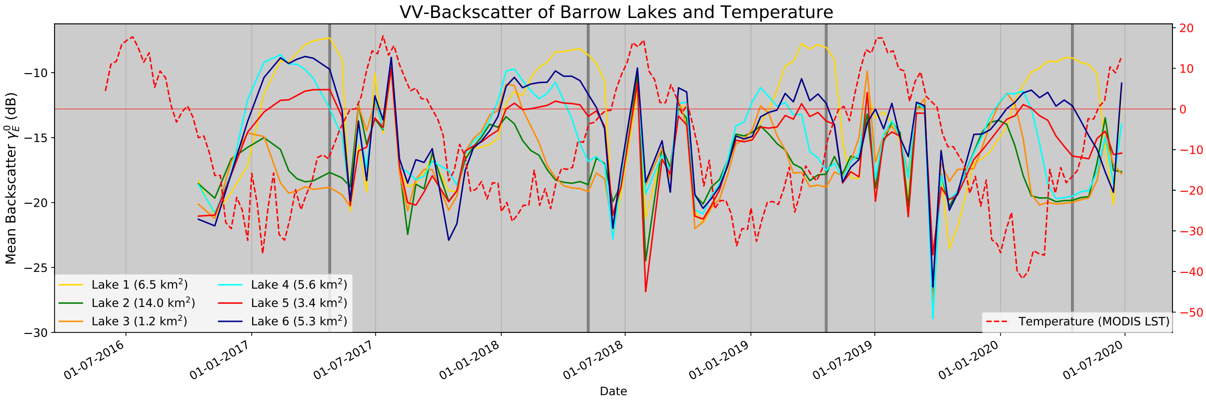

FIGURE 5.3: Barrow: Variations of mean lake surface γ_E^0 VV backscatter from 2016 to 2020. MODIS LST 8-Day temperature data represents is the average of the whole region. Colors of the backscatter line plots correspond to the the lakes marked in Figure 5.2. Bold vertical lines mark scenes that were selected for the yearly classification maps (see Table 4.1 in Section 4.4).

Our selection in Barrow (see Figure 5.2) includes 6 lakes ranging in size from 14.0 (Lake 2) to 1.2 km^2 (Lake 3). Looking at their VV backscatter time series in Figure 5.3, we can see that during the periods the lakes experienced temperatures above the freezing point, backscatter intensity changes were relatively uniform in direction (not necessarily magnitude) among the lakes, as they experienced different weather conditions. These changes do not tell us anything in the grand scheme, as they are merely a result of the exact timing of Sentinel-1 snapshots after each 12 days interval, given the fact that wind conditions were constantly changing. More interesting are the periods when temperatures fell far below the freezing point, which is usually the case from October to May. Here we can see that, after a delay of about two months, backscatter starts to first rise uniformly as the floating lake ice grows in thickness. Then after another 1-3 months, backscatter of our lakes start to split up. The backscatter of Lake 1 always continued to rise until temperatures started to approach 0°C again at the end of the season, which tells us that this lake must have the highest average depth from our selection, as the reflective ice-to-water transition stayed intact as the ice grew in thickness. Lake 2 and 3 showed a completely different backscatter behaviour, exhibiting the typical backscatter intensity drop expected from grounding ice as described by Jeffries et al. (1993). These lakes must be very shallow, as the ice grounded over the entirety of their surface areas. (See backscatter drop of Lake 2 in Figure 5.1). Lakes 4 to 6 are probably the most interesting candidates, since they exhibited varying backscatter behaviours for each cold season. The backscatter of Lake 4 showed hardly any drop in 2017, indicating that only a small fraction of its area was shallow enough to form grounded ice that year. In 2018 and 2019, the lake started to exhibit a larger drop in backscatter towards the end of the season, which suggests that a larger fraction of its area grounded. In 2020 it even reached the same backscatter floor of nearly -20 dB as Lake 2 and 3, which means that the ice grounded over its whole area , as shown in Figure 5.2. Parts of Lake 5 appear to ground very early in the season, as its backscatter intensity always stayed below -11 dB. Only in 2020 larger amounts of its ice cover started freezing onto its bed. Lake 6 never showed the typical backscatter drop that the other (partially) grounding lakes exhibited but rather a light and more gradual decrease in backscatter throughout the season.This indicates that small parts of it started to ground relatively early, while most of its bed stayed too deep for the ice to reach. Looking at Figure 5.3, we can see that the lake ice seems to have grounded more in 2020 than in previous years, hinting towards more ice growth in that year. This also correlates with the temperature curve that went below -40°C, a mark that was never broken in the three years before. In 2017 on the other hand, there was relatively little ice growth. Overall, we see a positive ice growth trend over the last 4 years in Barrow.

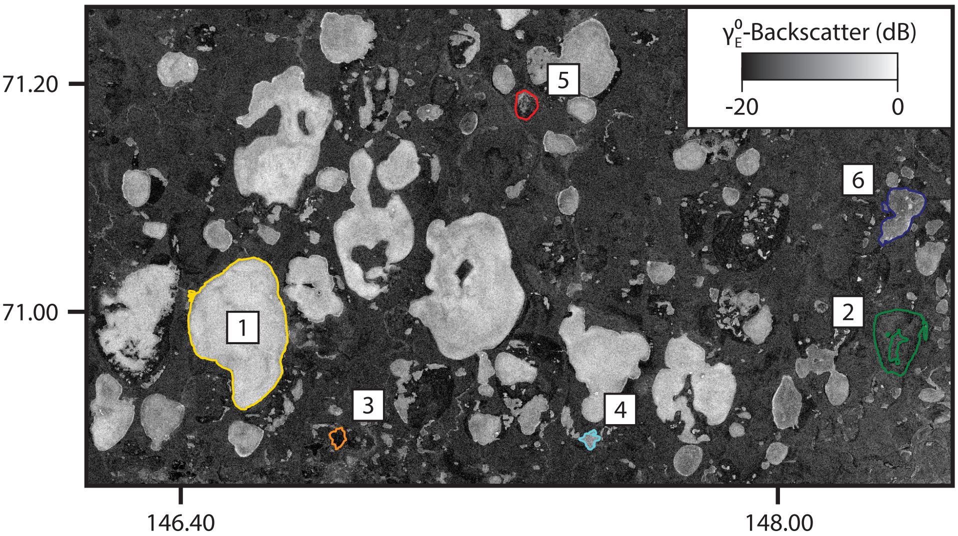

FIGURE 5.4: Kytalyk: IW VV polarised γ_E^0 backscatter image from 12.04.2020 (EPSG:32655) with marked selection of lakes (1-6) used for the determination of the annual ice maximum (see Section 4.4).

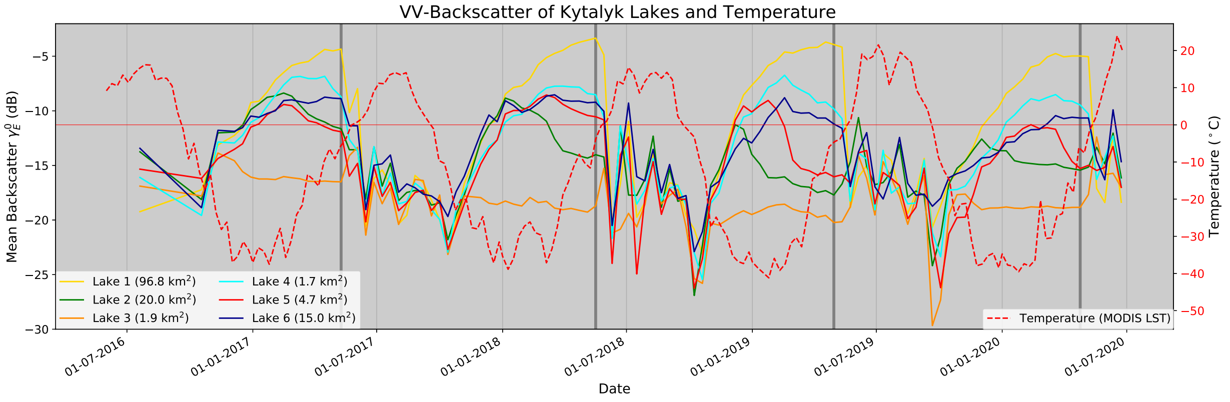

FIGURE 5.5: Kytalyk: Variations of mean lake surface γ_E^0 VV backscatter from 2016 to 2020. MODIS LST 8-Day temperature data represents the average over the whole region. Colors of the backscatter line plots correspond to the the lakes marked in Figure 5.4. Bold vertical lines mark scenes that were selected for the yearly classification maps (see Table 4.1 in Section 4.4).

As we have seen in Section 2.1, both the study site itself, as well as its lakes are on average much larger in Kytalyk compared to Barrow (see Figure 5.4). Our largest lake, Lake 1 (*Ozero Khantagay*) has a surface area of 96.8 km^2, while the smallest of our selection (Lake 4) is 1.7 km^2 in size. The backscatter intensity time series of our selected lakes (see Figure 5.5) show a very similar behaviour to Barrow with uniform, seemingly random changes during the warmer season and a diversification during the cold season. Lake 1 is the only lake, that showed no signs of grounding in any of the 4 observed icy seasons, reaching peak brightness of over -4 dB, which is about 4 dB higher than the highest average lake backscatter we observed in Barrow. We assume that this higher backscatter of floating ice in Kytalyk means that the ice was overall thicker than in Barrow. The temperature curve further supports this theory, as we were approaching temperatures of -40 °C much more consistently and for a longer period per season in comparison to Barrow. In 2017, Lake 2 (*Ozero Khosukun*) showed a rather late backscatter drop (February), which hints at a partial grounding of its floating ice cover. In 2018 and 2019 the grounded area further increased, as the backscatter drops started earlier (end of December, early January) and approached -18 dB in 2019, indicating that the ice was approaching a fully grounded state. In 2020 we see a slight decrease again in minimum backscatter intensity: While the initial drop occurred very early again, it stagnated midway through March. This could be due to the temperatures rising much earlier that year, resulting in a slowdown of ice growth. Lake 3 is the only lake that formed grounded ice throughout all winters. Its ice already started to ground early November and the corresponding backscatter reached minimum intensity quickly, lettig us assume that this lake is extremely shallow. Lake 4 exhibited little evidence of grounding, except in 2019, when a significant fraction of its ice cover started to ground in mid-February. This lake must therefore have a significantly higher average depth than Lake 2. The remaining lakes (5 and 6) are between Lake 2 and 4 in terms of their average backscatter intensity, with Lake 5 showing significant amounts of grounded ice in 2019 and 2020. Lake 6, even on the backscatter-rise, shows values that are generally lower than the ones of other lakes. This is a hint that a section of the ice grounded gradually in shallow waters, while the backscatter intensity of its still floating ice cover fraction increased. Only in 2019, the lake exhibited a trend towards significant grounding. Judging by this time series, Kytalyk seems to have shown an annual increase in annual ice growth from 2017 to 2019, with a slight decrease from 2019 to 2020.

5.2 Correlation with Sentinel-2 green band Surface Reflectance (SR)

In the previous section, we have shown that the typical backscatter drop associated with grounded ice is detectable at both of our primary study sites. This means that there are lake areas that were shallow enough for the ice to reach the bottom. In this section we attempted to investigate the average lake depth of our lake selection (see Figures 5.2 and 5.4) using the Sentinel-2 green band (Band 3). Duguay and Lafleur (2003) showed that (during summer) measured radiance values of the Landsat TM (Thematic Mapper) green band showed strong inverse correlation with SAR backscatter and could be calibrated with *in situ* measurements to obtain bathymetric maps of the Churchill lakes, Canada. Specifically, lakes with low SAR backscatter (grounded ice) showed higher radiance in the green spectrum compared to lakes with high backscatter (floating ice). This is caused by the decreasing translucency of the lake water and therefore its higher absorption of green light with increasing depth. While Band 3 of Sentinel-2 has different centre wavelengths (559 nm S-2A, 559.8 nm S-2B) compared to Band 2 of Landsat TM (570 nm), which Duguay and Lafleur (2003) had used, we still expected it to work well, as this lake depth investigation method is not particularly wavelength sensitive. Before we investigated this correlation at our primary study sites, Barrow and Kytalyk, we first looked at our secondary study site, Churchill - the same site that Duguay and Lafleur had used in their study - in order to see whether we are able to see the same correlation using more recent scenes from different SAR and optical sensors. In order to do this, we selected a cloudless Sentinel-2 scene from 30.07.2019 and a Sentinel-1 IW VV-pol scene from 07.04.2020 when we expect grounded ice to be clearly visible. As we did for Barrow and Kytalyk in Section 5.1, we also selected 6 lakes of different sizes (see Figure 5.6) to represent the Churchill lakes in our scatter plot (see Figure 5.7).

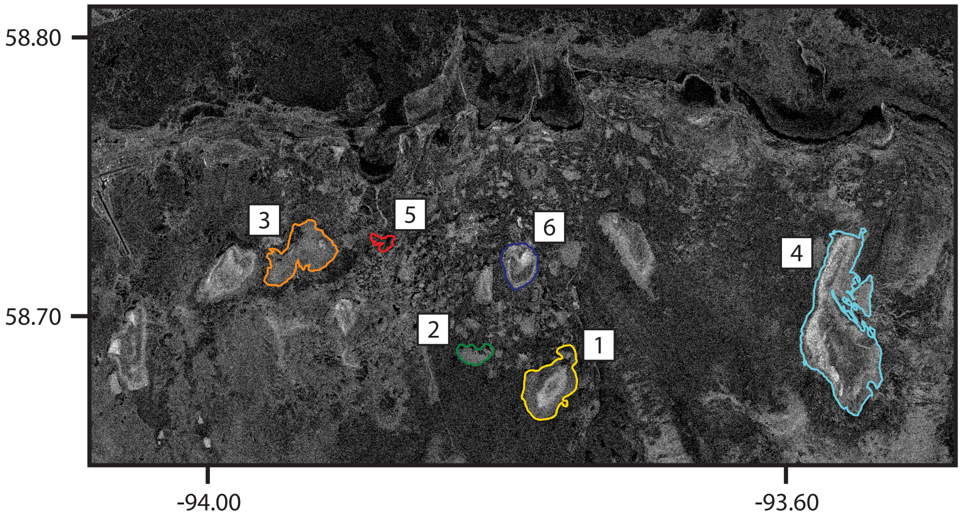

FIGURE 5.6: Churchill: IW VV polarised γ^0_E backscatter image from 07.04.2020 (EPSG:32504) with marked selection of lakes (1-6). JRC Yearly Water Classification History 2019 was used as the lake mask.

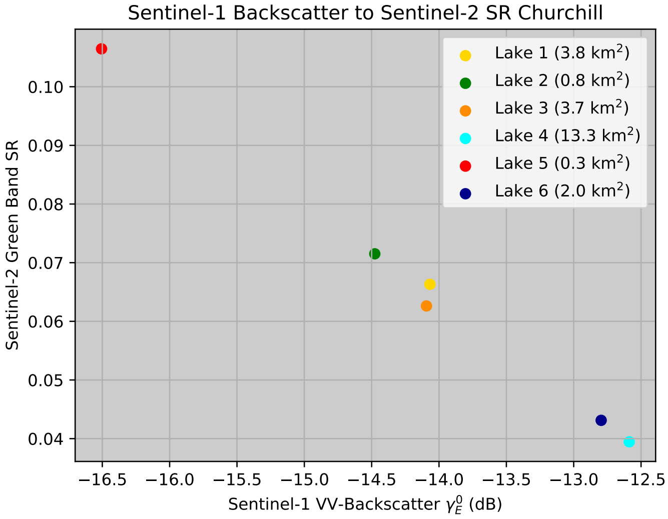

FIGURE 5.7: Sentinel-1 green band (Band 3) Surface Reflectances (SR) of the Churchill lakes plotted against their γ_E^0 backscatter. The lake numbers and colors correspond with the lakes marked in Figure 5.6. The Sentinel-2 image used for this analysis was acquired on 30.07.2019. The used IW VV-polarised Sentinel-1 scene is from 07.04.2020 (relative orbit number 19). Depicted values of both SR and γ_E^0 backscatter is the average calculated over each respective lake surface area.

Looking at the scatter plot (Figure 5.7), we can see that for Lake 5 which has by far the highest green SR value of our selected lakes (0.11), Sentinel-1 also measured the lowest backscatter in winter (-16.51 dB), indicating that this is a particularly shallow lake. Conversely, Lake 4 (*Norton Lake*) where the highest average backscatter intensity was measured (-12.59 dB), SR in the green spectrum detected by Sentinel-2 is the lowest (0.04). This means that this lake must be the deepest among our lake selection. Lakes 1, 2, 3 and 6 are arranged nearly perfectly in a straight line between Lake 5 in the top left and Lake 4 in the bottom right in the scatter plot. The correlation that Duguay and Lafleur (2003) discovered at this site using VV-polarised ERS-1 images and Landsat TM can therefore also be observed today, using IW VV-polarised Sentinel-1 scenes and Sentinel-2 MSI.

Refocusing onto our main study sites, we now look at the SR results in Barrow (see Figure 5.8, left plot). The lakes with the lowest measured backscatter (Lake 2 and 4, -18.85 and -17.97 dB) show the highest SR values (0.040 and 0.037). Lakes 3 and 5 which, although slightly less, are also grounded to a significant percentage (-17.30 and -16.04 dB), show much lower average green SR values (0.026 both) compared to Lakes 2 and 4. From thereon however, the inverse correlation collapses completely with Lake 6 which had much more floating than grounded ice (-13.08 dB): it shows a higher green SR value than Lake 3 and Lake 5 of 0.034. Lake 1 which has no floating ice at all (-10.38 dB), shows a green SR value that is even higher (0.036).

In Kytalyk, the data points in the scatterplot look random (see Figure 5.8, right plot). Lake 3, which has the lowest mean backscatter (-17.68 dB) and therefore must have had the most grounded ice only shows the fourth highest green SR from all 6 observed lakes. Lakes 2 (*Ozero Khosukun*) and

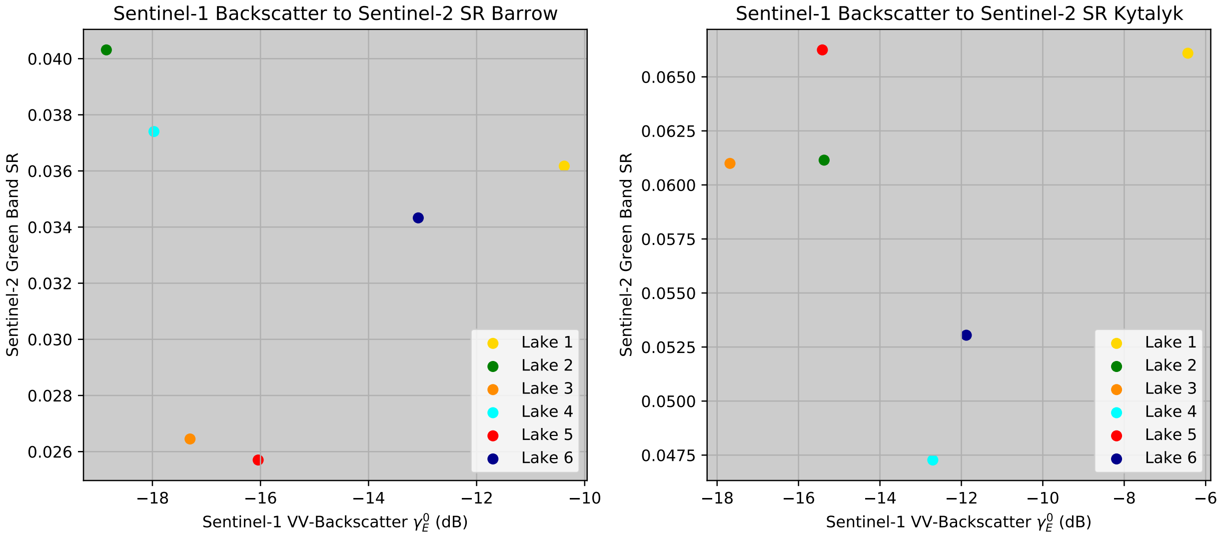

FIGURE 5.8: Sentinel-1 green band (Band 3) Surface Reflectances (SR) of the Barrow (left) and Kytalyk lakes (right) plotted against their γ_E^0 backscatter. The lake numbers and colors correspond with the lakes marked in Figure 5.2 (Barrow) and 5.4 (Kytalyk). The Sentinel-2 images used for this analysis were acquired on 11.07.2019 (Barrow), 16.08.2019 (Kytalyk, Lakes 1 and 3) and 13.08.2019 (Kytalyk, Lakes 2,4,5 and 6). The used IW VV-polarised Sentinel-1 scenes are from their respective 2020 ice maxima (see Table 4.1). Depicted values of both SR and γ_E^0 backscatter is the average calculated over each respective lake surface area.

5 which both appear with almost the same backscatter intensity in the Sentinel-1 images (-15.37 and -15.41 dB) show SR values in the green spectrum (0.061 and 0.66) that are both higher than the SR value of Lake 3. The partially grounded but mostly floating ice containing Lakes 4 and 6 (-12.70 and -11.88 dB) appear significantly dimmer in the green spectrum (0.047 and 0.053), but in reversed order. The most extreme outlier however is Lake 1 (*Ozero Khantagay*) which has by far the highest backscatter value of our selection (-6.44 dB) but also the second highest green SR (0.066).

Seen over both study sites, it is apparent that we were unable to detect the same clear inverse correlation between backscatter and green SR. While the correlation appears to somewhat hold up for lakes with lower γ_E^0 backscatter intensities - especially in Barrow - the higher the average backscatter of the lakes get, the less connection we can see between those two measurements. In additional experiments we conducted in the frame of this work (which we do not discuss in detail) we examined the SR of Sentinel-2 images with different acquisition dates and also Landsat 8 OLI scenes. We found that SR values differed greatly between the examined scenes, especially for lakes with high average backscatter values such as Lake 1 in Kytalyk (*Ozero Khantagay*). Looking at Figure 5.9 we can clearly see the cause of this: the water of the lakes in Barrow and especially also in Kytalyk show varying degrees of turbidity. Because of turbulences in the water, the spectral appearances of these lakes can change drastically even over short periods of time. In Churchill on the other hand, the water is clear enough for this bathymetry detecting method to work. Unfortunately, this means that we were unable to derive ice thickness from our lake ice classifications in this work.

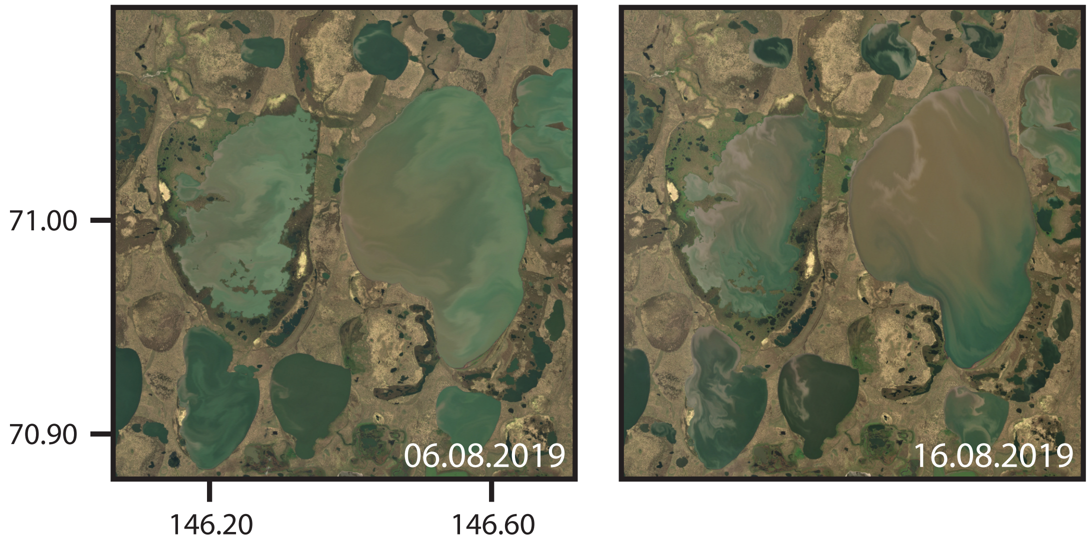

FIGURE 5.9: Sentinel-2 SR products (EPSG:32655) from 06.08.2019 and 16.08.2019 showing the lakes *Ozero Symytyr* (left) and *Ozero Khantagay* (right, Lake 1 in Figure 5.4) in visible colors.

5.3 VV and HH based classifications

In literature, both HH (Arp et al., 2011; Duguay et al., 2002) and VV polarised SAR images (Duguay and Lafleur, 2003; Jeffries et al., 1993) were successfully used to distinguish and map grounded and floating ice in subarctic regions, but they were usually not compared side by side. Due to our fortunate data situation (see Section 4.1), we were able to assess the consistency of our results based on either polarisation in this section. For this section, we took a look on how the maximum percentage of grounded ice had changed over the last 4 years. These annual classifications were done using the images we identified as the ones depicting the ice maximum for each year (see Section 4.4). Note that there are varying acquisition time differences between each of the annual HH and VV polarised scenes selected for these classifications (see Table 4.1). As we did in the previous section, we first look at our results of the Barrow region, before we move on to Kytalyk.

TABLE 5.1: Barrow: Yearly fraction of grounded ice (GI) of the whole lake ice area (**331.6** km^2) derived from VV- and HH-based threshold classifications. Δ GI is the observed change in grounded ice percentage from the previous year. Note that values in *italic* describe changes over two years, as no HH-polarised data was available for 2018. OC is the Overall Consistency between the VV and HH-based classifications. See Table 4.1 for exact dates used and Table 4.2 for applied thresholds for each polarisation.

	VV GI (%)	VV ΔGI (%)	**HH GI (%)**	HH ΔGI (%)	**OC (%)**	ΔOC (%)
2017	**35.42**		**32.53**		**92.74**	
2018	**39.00**	+ 3.58	**-**	-	**-**	-
2019	**38.88**	- 0.12	**35.6**	+ *3.07*	**91.89**	- *0.85*
2020	**48.54**	+ 9.66	**44.21**	+ 8.61	**90.63**	- 1.26

Looking at the VV based classification of Barrow's lake ice first (see Table 5.1), more than two thirds of our study site's lake ice was classified as grounded ice in 2017. First, we can see a clear increase of more than 3% from 2017 to 2018. From 2018 to 2019, the total grounded ice area stayed more or less the same, with a minuscule 0.12% drop from the previous year. This small change must not be taken at face value though, as a shift of a few days of the 12 days temporal resolution could have potentially been enough to reverse the direction of this change. From 2019 to 2020 though, we observed a very significant increase of 9.66% in grounded ice, with its total area reaching 48.54% of the whole lake surfaces. Overall, there is an increase in grounded ice occurrence over this 4 year time period, matching the observations we made in the previous Section (5.1).. For our HH based classification we unfortunately had no EW data available for 2018, but the same the same positive grounded-ice-trend as with the VV based classification is visible also here. However, the HH based classifications gave us generally lower values for grounded ice compared to the HH based ones. Interestingly, this discrepancy systematically increases in tandem with the growing grounded ice fraction over the years. In 2017, the HH based classification detects -2.89% grounded ice compared to the VV based one, which then grows to -3.28% in 2019 and finally to -4.33% in 2020. This connection is reflected in the overall consistency values of these classifications, which naturally also decline with the increasing discrepancy. However, all consistencies still remain above 90%, indicating that our VV and HH based classifications of the Barrow site are well comparable overall.

TABLE 5.2: Kytalyk: Yearly fraction of grounded ice (GI) of the whole lake ice area (**1676.6** km^2) derived from VV- and HH-based threshold classifications. Δ GI describes the observed change in grounded ice percentage from the previous year. OC is the Overall Consistency between the VV and HH-based classifications. See Table 4.1 for exact dates used and Table 4.2 for applied thresholds for each polarisation.

	VV GI (%)	VV ΔGI (%)	**HH GI (%)**	HH ΔGI (%)	**OC (%)**	ΔOC (%)
2017	**5.99**		**5.61**		**95.48**	
2018	**7.96**	+ 1.97	**6.96**	+ 1.35	**95.34**	- 0.14
2019	**13.92**	+ 5.96	**12.29**	+ 5.33	**94.19**	- 1.15
2020	**10.59**	- 3.33	**9.52**	- 2.77	**94.84**	+ 0.65

Moving on to our classification results of Kytalyk, (see Table 5.2), we find that the determined fractions of grounded ice are much lower than in Barrow, never exceeding 15% of its much larger total lake surface area. The VV based classification shows an increase of grounded ice area of nearly 2% from 5.99 in 2017 to 7.96% in 2018. In 2019 we register the highest fraction of grounded ice of 13.92%, which is a relatively large increase of nearly 6% from the previous year. To 2020 we then finally observe a decrease in bedfast ice of 3.33% to a total fraction of 10.59%. This general increase of grounded ice from 2017 to 2019 and subsequent decrease again matches exactly with what we saw in its corresponding backscatter time series in Section 5.1. Looking at the results from the HH based classification, they are again generally lower and show the same systematic discrepancy as in Barrow, meaning that the difference between the VV and HH based classification increases and the overall consistency decreases with the grounded ice fraction getting larger. Just as the grounded ice percentage is generally lower in Kytalyk compared to Barrow, the differences are also smaller, always staying beneath 2%. Consequently, the overall consistency between the two classifications is generally higher with very good values between 95.48 in 2017 and 94.19% in 2019. These better consistencies are certainly related to there being generally less grounded ice than in

Barrow, as producer's consistency for grounded ice have less of a consequence to the overall consistency. Exemplary, the excellent comparability can be nicely seen looking at *Ozero Khantagay* (see Figure 5.10). The higher detailedness coming from the higher resolution of 10m of the IW VV- compared to the 40m of the EW HH-polarised scenes are clearly visible in the corresponding classifications. The different resolutions undoubtedly contribute to lowering the overall consistency between the two classifications, however we can also clearly see that the general regions where grounded or floating ice dominate match up well.

Overall, looking at both regions we can see that VV and HH based classifications are quite consistent. Both capture the same annual grounded ice developments and trends. Also visually, the resulting maps match up very well considering they stem from different acquisition modes and native GSDs. There is however a discrepancy between the two polarisations with VV based classifications always giving us the higher numbers for the grounded ice fraction, but the differences do show a systematic component, and they are therefore - to an extent - predictable: We can for example approximate our HH based results in Tables 5.6 and 5.7 by multiplying the corresponding VV based grounded ice percentages by 0.9 and were able to match the true values within a range of roughly ±0.24%.

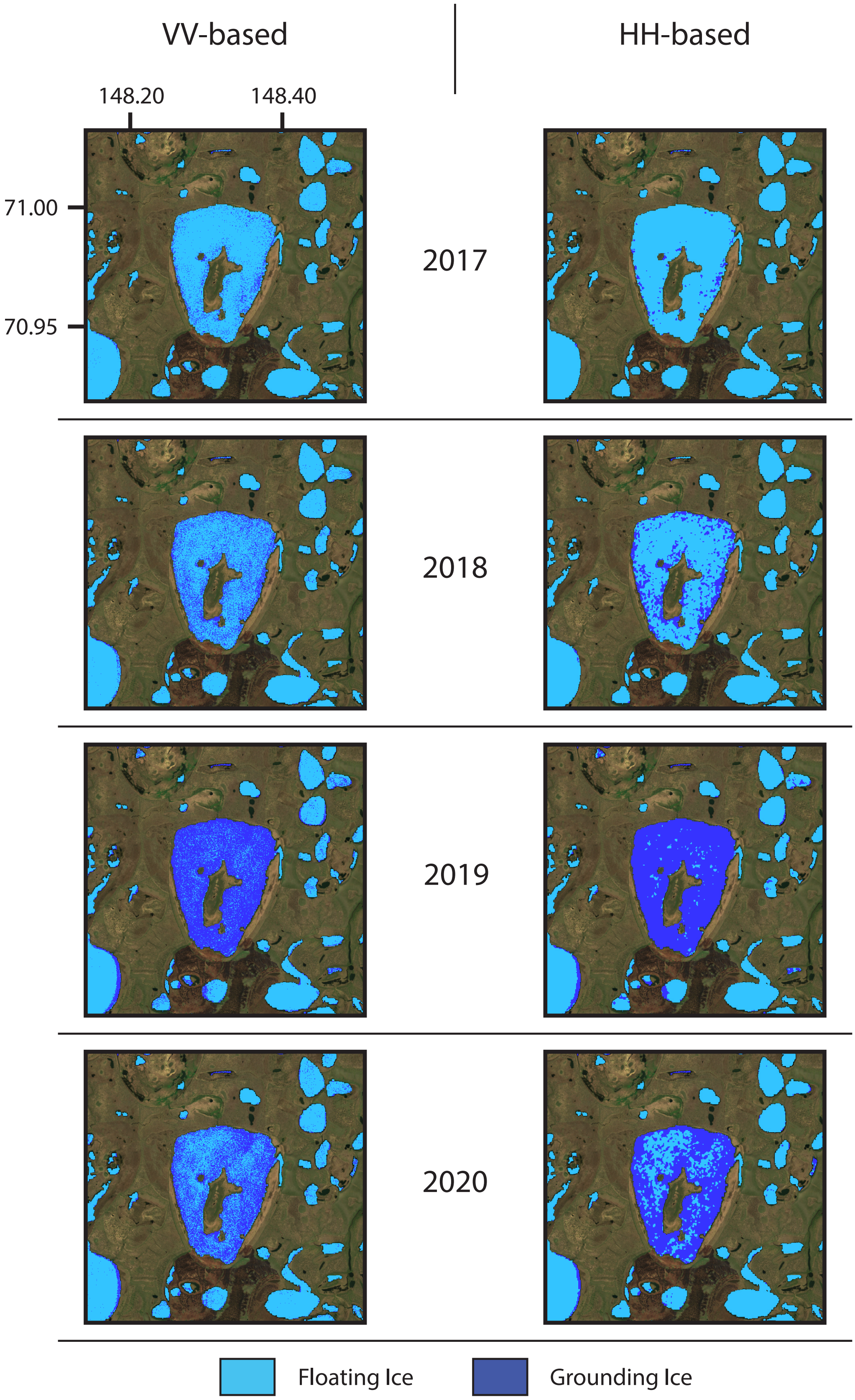

FIGURE 5.10: Annual classifications based on VV and HH for Ozero Khosukun in Kytalyk. The underlying Sentinel-2 image was acquired on 13.07.2020 (EPSG:32655).

5.4 Correlation with ECMWF ERA5 climate data

As we have seen, the results from the co-polarisatrion based classifications are quite consistent. This alone however does not yet give us certainty concerning the credibility of these results. If they in fact do show grounded ice, we should expect a strong correlation with the temperature and weather data of their respective study sites, as the grounding of ice is dependent on ice cover thickness. We have already briefly looked at the MODIS LST temperatures in Section 5.1 and have found some possible connections between the temperatures and the backscatter progressions. Ambient air temperature however is by no means the only significant influence on lake ice growth as has been shown by Surdu et al. (2014) amongst others. Especially snow cover thickness is also an important factor to consider, as it impedes the flow of thermal energy from the lake ice surface to the cold arctic air, therefore slowing down further growth of the lake ice, which subsequently leads to less grounded ice formation. The ECMWF ERA5 climate reanalysis data set gives us the opportunity to investigate the climatic context of our classifications more thoroughly, as it contains not only temperature, but also information on precipitation and wind, which can give us a hint on relative snow cover thickness changes between the years.

In the following analysis, we compared the results we presented in the previous Section (5.3) with ECMWF ERA5 climate reanalysis data. Specifically, we looked at the average daily mean temperatures from October to May, which is the period in which ice formation and growth occurred at both sites, as we have seen in Section 5.1. In addition to that, we also took the snowfall that occurred between 3 months prior up to the date of our classification into account. As a third parameter, we also included wind speed, which was calculated from the u and v components included in the ERA5 dataset, in order to estimate how well the snow was able to accumulate. Note that the denoted wind speed values in Table 5.3 and 5.4 appear to be low as they were averaged over the same 3 months period, which means that peak wind speeds were multiple orders of magnitude higher. Because we have already presented the relationship of the two co-polarisation based grounded ice classifications in the previous section, we only reference the VV-based classification in this section. Like we did in the previous two sections, the focus is first on the Barrow study site, before we move on to Kytalyk.

TABLE 5.3: Barrow: Correlation of the maximum VV based grounded ice fraction (GI) we detected for each year with ECMWF ERA5 climate reanalysis data. Temperature (T) is the October to May average of the daily mean temperature that was calculated for the region. Snowfall (S) indicates the precipitation that fell from three months prior up to the acquisition date of the corresponding SAR image on which the respective classification is based on (see Table 4.1). Wind-speed (W) is the daily average wind-speed calculated for the same 3 months time-frames as Snowfall. Δ always denotes the difference from the previous year.

	VV GI (%)	VV ΔGI (%)	**T (°C)**	ΔT (°C)	**S (mm)**	ΔS (mm)	**W (km/h)**	ΔW (km/h)
2017	**35.42**		**- 13.14**		**42.21**		**2.24**	
2018	**39.00**	+ 3.58	**- 12.34**	+ 0.80	**51.84**	+ 9.63	**11.72**	+ 9.48
2019	**38.88**	- 0.12	**- 12.75**	- 0.41	**55.98**	+ 4.14	**8.72**	- 3.00
2020	**48.54**	+ 9.66	**- 15.24**	- 2.94	**43.29**	- 12.69	**5.01**	- 3.71

Looking at the temperatures (see Table 5.3), we see that they ranged from -12.34 in 2018 to -15.24°C in 2020. The coldest year 2020 does match up with the highest amount of grounded ice (48.54%) in 2020, however, things are not as obvious for the other years. In 2017, when we would have expect the warmest temperatures based on the low fraction of grounded ice (35.42%), temperatures were the second to lowest in this annual time series (-13.14°C). If we additionally only take snowfall into account, this seems to disagree even more with our classification, as for 2017 there was only 42.21 mm of snowfall calculated by ECMWF, which is more than 9.5 mm less snow than in the following year, where more grounded ice was detected. However, it was also by far the least windy year within this time period, with only 2.24 km/h on average. Therefore taking wind speeds into account, this means that the snow accumulated more in that year, even though Barrow experienced the least amount of snowfall compared to the following 3 years. This led to comparatively less lake ice growth than we would otherwise expect. Winter 2018 was the warmest period in our series, with daily mean temperatures of -12.34°C and more snowfall (51.84 mm) than in 2017. However ECMWF calculates by far the highest wind speeds with 11.72 km/h, which is a big increase from the calm previous year. This wind must have scattered large amounts of snow, preventing it from accumulating more. This combination therefore seems to have led to a respectable increase of 3.58% of grounded ice, despite the higher temperatures. In 2019, where we identified a very similar amount of grounded ice as in the previous year (38.88%), the temperatures were slightly colder with -12.75°C. However, there was also more snowfall (55.98) and less wind (8.72 km/h). The 2020 winter is by far the clearest case to interpret, as Barrow experienced not only the lowest temperatures (-15.24°C), but also less snowfall compared to the two previous years (43.29 mm). The 3.71 km/h decrease in average wind speed compared to the previous year was clearly not large enough to prevent the formation of the thickest lake ice cover in 2020. Thus, taking all three climate parameters into consideration, we can see a correlation in Barrow between grounded ice formation and ERA5 climate data, which adds credibility to the classifications.

TABLE 5.4: Kytalyk: Correlation of the maximum VV based grounded ice fraction (GI) we detected for each year with ECMWF ERA5 climate reanalysis data. Temperature (T) is the October to May average of the daily mean temperature that was calculated for the region. Snowfall (S) indicates the precipitation that fell from three months prior up to the acquisition date of the corresponding SAR image on which the respective classification is based on (see Table 4.1). Wind-speed (W) is the daily average wind-speed calculated for the same 3 months time-frames as Snowfall. Δ always describes the difference from the previous year.

	VV GI (%)	VV ΔGI (%)	**T (°C)**	ΔT (°C)	**S (mm)**	ΔS (mm)	**W (km/h)**	ΔW (km/h)
2017	**5.99**		**- 18.53**		**33.39**		**6.53**	
2018	**7.96**	+ 1.97	**- 20.25**	- 1.72	**36.45**	+ 3.06	**6.48**	- 0.05
2019	**13.92**	+ 5.96	**- 20.97**	- 0.72	**26.46**	- 9.99	**7.26**	+ 0.78
2020	**10.59**	- 3.33	**- 20.60**	+ 0.37	**31.50**	+ 5.04	**9.72**	+ 2.46

Focusing on the Kytalyk study site (see Table 5.4), temperatures are much lower than in Barrow, with the highest mean daily average temperature in 2017 of -18.53°C being more than 3°C colder than the coldest temperatures in Barrow (-15.24). In addition, there was generally much less snowfall and also more consistent wind conditions over the last 4 years. Only the most recent year, 2020 showed a notable increase in wind speed (+2.46 km/h). We can therefore safely ignore the small wind speed changes of the first 3 years. In 2017, temperatures were the highest with -18.53°C, and unsurprisingly, our classification also mapped the least amount of grounded ice (5.99%). In the following year, average winter temperatures dropped by 1.72°C to -20.25°C. Compared to this temperature drop, the slightly increased snowfall (36.45 mm) appears to have been less impactful, as we detected an increase of nearly 2% in grounded ice area. In 2019, grounded ice fraction in Kytalyk was the highest (13.92%) . This was an increase of nearly 6% from the previous year. The decrease in average temperature from the previous year of 0.72 to -20.97°C is relatively small, however ECMWF also calculated snowfall of only 26.46 mm for this period in 2019, which is just shy of 10 mm less than in the previous season. The combination of very cold temperatures and little snowfall must have therefore strongly boosted ice growth. Finally in 2020, there was a small increase in mean temperature of 0.37 to 20.6°C, which also corresponds to the lower percentage of grounded ice (10.59%) in our classification. This decrease might have also been slightly amplified by the notable increase of more than 5 mm in snowfall. However, this effect was also lessened by the distinctive increase (+2.46 km/h) in average wind speed. Overall, the temperature changes appear to have been the main driver of ice growth in Kytalyk. In Barrow on the other hand, snowfall and wind had more importance, as there was in general more snow and more annual variability in snowfall as well as in the average wind speed. The Kytalyk thermokarst lakes must be on average significantly deeper compared to the ones in Barrow, as even with significantly colder conditions and less substantial snow cover, we detected much less grounded ice than in Barrow. This observation corresponds with the higher backscatter Sentinel-1 detected on floating ice in Kytalyk versus Barrow, suggesting that the floating ice must have been thicker (see Section 5.1).

Overall, we can say that our co-polarisation based results look plausible given the climatic circumstances. However, we want to make clear, that this highly interpretative analysis without any weighting of the different factors and no statistical support, is by no means a replacement for a comparison with a physical lake ice model, as it was used by Duguay and Wang (2019) to assess the accuracy of their own classifications.

5.5 VH and HV based classifications

As we have seen in the previous sections, co-polarised Sentinel-1 data worked well for mapping grounded ice in Barrow and Kytalyk and the resulting classifications were very comparable, with overall consistencies always staying above 90%. Basing grounded ice classifications on VH and HV polarised data is, however, much more experimental. As we already mentioned in Section 4.5, finding the right threshold values proved to be much more challenging for the cross-polarised bands compared to the co-polarised ones, as the histograms of the masked lakes showed barely any notable separation into the two groups (high backscatter = floating ice, low backscatter = grounded ice) which were easily discernible in the co-polarised data. We therefore have to keep in mind that the following results come with high uncertainty, as our confidence in the employed thresholding method in combination with cross-polarised data is low.

Looking at our results for both study sites in Table 5.5, we see that the values we got for the

TABLE 5.5: Annual maximum fraction of grounded ice (GI) of the whole lake ice areas (**331.6** km^2 in Barrow and **1676.6** km^2 in Kytalyk) derived from VH- and HV-based threshold classifications including Overall Consistencies OC for each cross-polarisation based classification with its corresponding co-polarisation based classification, which is VV for VH (IW) and HH for HV (EW). OC values are related to the respective classification type to their left.

	Barrow				Kytalyk			
	VH GI (%)	OC (%)	HV GI (%)	OC (%)	VH GI (%)	OC (%)	HV GI (%)	OC (%)
2017	-	-	34.63	89.46	10.07	93.04	3.42	96.72
2018	59.63	71.75	-	-	26.72	80.12	6.30	96.01
2019	64.52	68.30	33.98	90.47	33.44	77.52	8.10	92.78
2020	67.62	73.17	44.04	86.69	34.36	74.18	8.63	93.60

grounded ice fractions with the VH based classification are much higher than the ones determined with co-polarised backscatter data, while the HV based classification delivers values that are much more within the range of the co-pol results. Unlike when we compared the VV and HH classifications in Section 5.3, we calculated overall consistencies with their corresponding co-polarised counterparts, which measured the same active RADAR pulse backscatter and was acquired at the same time with the same acquisition mode, as this is where we would expect high consistencies to be most probable. Unsurprisingly, given the high discrepancy in detected grounded ice, overall consistency values of VH related to VV based classifications are with the exception of the classifications of 2017 in Barrow all well under 90%, going as low as 68.30% for the 2019 classification in Barrow. It is especially notable how strong the overall consistencies fluctuate from year to year and how, in contrast to the consistencies between the co-polarisation based classifications, their fluctuations are seemingly independent of increases or decreases in grounded ice area. This is most noticeable in Barrow, when overall consistency improves from 2019 to 2020 by 4.87% even though grounded ice area increased. The results from the HV based classification fit the HH-based ones much better, especially in Kytalyk, where there was less grounded ice, overall consistencies are all over 92%. In Barrow however, they only manage to break over 90% in the 2019 classification.

Comparing all our resulting ice fractions (see Figure 5.11), it becomes apparent, that for both cross polarisation based classifications, regardless of the deviations in absolute grounded ice fraction within the same year, inter annual changes also do not match up with the HH and VV based ones. While the VV and HH based classifications show a clear decrease of grounded ice area from 2019 to 2020 (VV -3.33%, HH -2.77%), both VH and HV register small increases instead (VH +0.92%, HV +0.53%). We can also find a similar situation looking at the VV and VH based classifications in Barrow from 2018 to 2019, where VV detects about the same amount of grounded ice (-0.12%), while VH shows quite a big increase (+2.89%). The opposite disagreement can be seen looking at the HV based classification in Barrow from 2017 to 2019: the slight decrease of grounded ice detected with HV (-0.65%) contradicts with the increase in grounded ice detected by the co-polarisation based classifications (VV +3.58%, HH +3.07%).

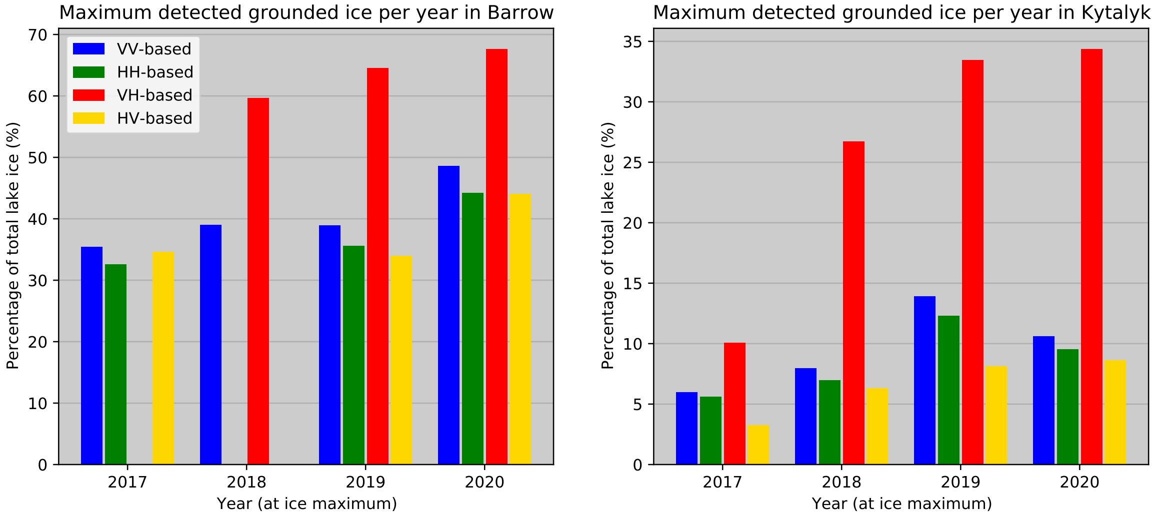

FIGURE 5.11: Comparison of the classified grounded ice fractions based on all 4 polarisation modes for both study sites. Visualised data correspond with values in Tables 5.1, 5.2 and 5.5.

5.6 Comparison with Duguay and Wang (2018)

In this Section we present our results from the accuracy assessment with Duguay and Wang (2018). As we have already mentioned in Section 4.7, the comparison with this dataset can give us a hint on how accurate our results might be, because Duguay and Wang compared their results to lake ice model calculations in their accompanying Paper (Duguay and Wang, 2019) and deemed their threshold method (which is what we compare our results to here) as 92.56% accurate over all images they classified in their study. We therefore need to make very clear at this point that, while we call this an *accuracy assessment*, it is only the closest to one we were able to do and values in the following Tables 5.6 and 5.7 are not absolute accuracies to neither model calculations nor ground truth and should therefore also not be interpreted as such. The most interesting aspect about this comparison is, that Duguay and Wang - according to their denoted classification dates - must have used the same EW swaths we used here for these comparisons, which means that we can theoretically expect very high accuracies. This is because both their as well as our classification maps would be subject to the same residual image noise as well as any other potential errors coming from the Sentinel-1 data side. This is especially interesting in regards to to our set backscatter thresholds, as this was basically a test on how close we set our threshold compared to theirs. However, it also needs to be considered that Duguay and Wang did not include any detailed information on the exact method or polarisations they used to create these classification maps, and considering that the pixel density in their classifications are higher than the one from our EW GRDM based version, we have to assume that they either based their classification on the GRDH product of the same EW swath, as we stated in Section 4.7, or they used some unspecified algorithms in order to achieve sub-pixel resolution. Either way, we have to expect a certain percentage of the following deviations to originate from either one of those circumstances, as well as the resampling of our data that was needed on our side to fit their resolution.

TABLE 5.6: Barrow: Accuracy assessment of our classifications based on different polarisations using the data set of Duguay and Wang (2018) as our reference, including Producer's (PA) and User's Accuracy (UA) of both the Grounded (GI) and Floating Ice (FI) classes as well as the Overall Accuracy (OA). ΔGI describes the difference of our GI from the one from Duguay and Wang's classification (**29.94%**). Values in *italic* are not based on the Sentinel-1 acquisition as Duguay and Wang's classification.

Polarisation	**GI tot.** (%)	Δ**GI** (%)	FI UA (%)	GI UA (%)	FI PA (%)	GI PA (%)	OA (%)
HH	**32.68**	**+ 2.74**	95.19	99.58	99.81	91.23	97.01
HV	**34.70**	**+ 4.76**	89.13	90.51	95.65	78.09	89.56
VV	***35.45***	***+ 5.51***	*89.48*	*93.81*	*97.13*	*79.22*	*90.78*

We first compare our HH based classification from the 24.04.2017 with the one from Duguay and Wang (2018) of the same date (see Table 5.6). Duguay and Wang classified 29.94% of their pixels as grounded ice, while our HH based classification detected 32.68%, which is 2.72% more. Note that this fraction of grounded ice is slightly higher (+0.15%) than the one we observed for the same date and using the same polarisation mode in Section 6.2, Table 5.1 (32.53%). The reason is, that we used the same lake mask here as Duguay and Wang (see Section 4.6), which is less restrictive around the edges of the lakes where most grounded ice occurs compared to our JRC water occurrence based lake mask (see Section 4.3), which results in this slightly higher value. This is also evident looking at the total lake ice area of this lake mask, which is 333.3 km^2, 1.7 km^2 more than when we used our own one. Our achieved overall accuracy is high, with a value of 97.01% and producer's and user's accuracies for both classes staying well over the 90% accuracy threshold. Unsurprisingly, most deviations originate from the misclassification of floating ice as grounded ice, as we can see from the 91.23% producer's accuracy of the grounded ice class. This caused the user's accuracy (95.19%) to decrease as well, but not as strong, since there is was two times more floating than grounded ice in Barrow. As the remaining two accuracy values are both above 99% this means we have practically no noteworthy misclassifications of grounded as floating ice. This could indicate that we may were using a slightly higher backscatter threshold compared to Duguay and Wang. Moving to the HV based classification, which is also based on the same EW swath, we detected 2.02% more grounded ice compared to the HH based one and therefore overall accuracy is consequently also lower with 89.56%. Unlike with the HH based classifications, we can see a clear drop in user's and producer's accuracies of both classes. This indicates that there are misclassifications in both directions, even though still much more towards more grounded ice, where we have a producer's accuracy of 78.09%. Looking at this result, it looks rather improbable that Duguay and Wang incorporated HV backscatter into their classification process. Because the data availability allowed for it, we also included the VV based classification into our comparison, however, we have to be aware that it is not based on the same EW scene but rather on the IW swath acquired 1 day later. It was therefore unlikely, that we would reach same level of accuracy as with the HH based classification. As we already know from Section 6.2, VV based classifications detect higher percentages of grounded ice than, HH based ones, which in this case means that we see +5.51% grounded ice compared to Duguay and Wang (2018). This is an even higher discrepancy than we obtained with the HV based classification, but despite this, the overall accuracy is actually higher with 90.78%. Also, all individual class accuracy indicators are higher than the ones from the HV based classification, which means that, while we detected even more grounded ice, we mapped more of it in the correct places. In summary, we can therefore say that the VV based classification method worked better compared to the HV based one than the small increase in overall accuracy (+1.22%) would suggest. Also, most of the deviation in the amount of detected grounded ice could probably be improved by tuning the threshold value.

TABLE 5.7: Kytalyk: Accuracy assessment of our classifications based on different polarisations using the data set of Duguay and Wang (2018) as our reference, including Producer's (PA) and User's Accuracy (UA) of both the Grounded (GI) and Floating Ice (FI) classes as well as the Overall Accuracy (OA). ΔGI describes the difference of our GI from the one from Duguay and Wang's classification (**6.76%**).

Polarisation	**GI tot.** (%)	Δ**GI** (%)	FI UA (%)	GI UA (%)	FI PA (%)	GI PA (%)	OA (%)
HH	**8.93**	**+ 2.17**	97.54	98.26	99.87	74.36	97.59
HV	**5.88**	**- 0.88**	98.64	68.22	92.71	78.45	96.58

As we stated in Section 5.6, we used an EW scene from 20.04.2016 for our Kytalyk comparison with Duguay and Wang (2018), which lies outside of our 4 years investigation period. Looking at the HH based classification, we can see that it detected 2.17% more grounded ice than Duguay and Wang's, which is a very similar deviation as in Barrow, albeit slightly less. Correspondingly, our overall accuracy of 97.51% is even a little higher compared to the corresponding accuracy in Barrow. Similarly, we see a noticeable drop in the producer's accuracy of the grounded ice class, which means that nearly all of the grounded ice other than the 2.17% we detected additionally, have been mapped identically. This again indicates a simple upwards shift of our set backscatter threshold compared to Duguay and Wang's. While the producer's accuracy of grounded ice (74.36%) is noticeably lower than in Barrow (91.23%), this is expected, given that there is much less grounded ice in Kytalyk to begin with. A similar increase in detected grounded ice area is therefore much more noticeable. Moving on to the HV based classification, we can see that, in contrast to what we saw in Barrow with this polarisation, we detected 0.88% less grounded ice than Duguay and Wang did. This is the closest to their grounded ice amount in all these comparisons. However, it has a slightly lower overall accuracy (96.58%) than we achieved with the HH based classification. While the producer's accuracy of grounded ice and the user's accuracy of floating ice are higher (which is not surprising given the fact it detected less grounded ice), the remaining two accuracies are much lower than their respective values of the HH based classification. This again indicates, that we have false classifications in both directions. Unfortunately, we had no matching IW scenes available for Kytalyk (see Section 5.6), which means that we are unable to compare a VV based classification with Duguay and Wang's for this site. Given the overall high consistencies we observed between the co-pol based classifications in Section 6.2, we can assume, that it would have fared similarly, if not better than in Barrow, given that the discrepancy in detected grounded ice seems to be generally lower in Kytalyk due to its much lower occurrence at this site.

Overall, we can say that with our HH based classifications, we consistently came very close to Duguay and Wang's classification maps at both study sites. This is especially remarkable, as the backscatter threshold was based solely on the Barrow scenes but produced results in Kytalyk that are just as accurate as in Barrow. At both sites, for both comparisons that we conducted, the HH based classifications produced maps with more than 2 but less than 3% of the pixels *misclassified* as grounded ice. However, in Duguay and Wang (2019) they stated, that over all of their threshold based classifications, most of the errors compared to the lake ice model, came from the false classification of grounded as floating ice. Given that both co-pol based classifications show the opposite problem, we can assume that a good portion of this grounded ice surplus was classified at the correct location in our classification maps compared to the model calculations. Unfortunately, we have no way of telling how large this correctly classified percentage of our *misclassifications* is. Therefore, we also have no way of telling whether our classifications would have fared better or worse in an accuracy assessment with Duguay and Wang's lake ice model compared to their classifications (92.56%). However, considering that our HH based classifications are both overall more than 97% consistent with Duguay and Wang's, we can assume that they would have fared similarly well and most probably would have also produced an overall accuracy of over 90% in comparison with the lake ice model. We have however also seen, that our HV classification produced very inconsistent results between the two study sites, which also reflects the general inconsistencies we observed from the cross pol based classifications in Section 5.5. Whether these inconsistencies are mostly caused by actual interaction and subsequently caused polarity reversal of the RADAR signal with the ice, meaning that there is only limited correlation between cross-polarised backscatter and grounded ice, or are mainly caused by noise due to the threshold being set too low (NESZ), we are unable to tell with any degree of certainty. But we assume that both factors might play a role in this.

6 Discussion

6.1 The importance of accessible lake depth data

Ice thickness and lake depth are the two deciding factors of arctic lake ice regimes. If the ice thickness is larger than the lake depth, we have grounded ice, if on the other hand lake depth exceeds ice thickness, what we have is floating ice (Engram et al., 2018). Various climate factors have a direct influence on ice thickness, but only indirectly decide on the resulting ice regime (grounded or floating). This means, that without having a basic knowledge about lake depths, we are simply unable to properly quantitatively assess the influence of the climate on grounded ice formation. The directional changes (more or less grounded ice) can be taken at face value, even without knowing ice depth. However, small temperature increases could suddenly lead to a lot more grounded ice, as the freezing reaches a critical depth. We therefore have to be careful interpreting magnitudes in grounded ice changes between years, because as long as we do not know the bathymetry of the examined lakes we are missing an important link between the grounded ice area and the climatic variables (see Section 5.4).

For most studies on grounded ice in arctic lakes, researchers either themselves conducted probing (Duguay and Lafleur, 2003) or used data from pre-existing *in situ* lake depth measurements (Arp et al., 2011; Engram et al., 2018) in order to derive ice thickness from the ice classification maps. However, as subarctic thermokarst lakes are usually in very remote locations and are therefore often rather difficult to access, such probings typically come with great effort and cost. This consequently means that such measurements are done where access is logistically comparatively easier and that these probings are typically done only once but are then being referred to for decades, out of necessity. The potential hydrological and geomorphological changes that might have occurred in the meantime are ignored as a result of this. In addition, to interpolate further bathymetric information from these point measurements using lake ice SAR images, uniform ice thickness across the study area has to be assumed (Jeffries et al., 1996). This might not always conform with reality, especially at very large locations such as Kytalyk, where inter-local weather differences could start to matter. These above-mentioned constraints are probably some of the the major reasons for why, so far, nearly all detailed studies on grounded ice have been restricted to mostly the same couple of relatively well confined sites (like for example Churchill or Barrow), while most of the extremely expansive regions of northern Russia (such as Kytalyk) were hitherto ignored. However, in order to gain further understanding of how the physical processes in these subarctic wetlands influence and are being influenced by climate, being able to study ice regimes in a wider geographical context would certainly be beneficial.

The prospect of using remote sensing data for lake depth assessment instead of *in situ* point measurements is therefore extremely attractive, as it would not only get rid of site accessibility constraints, but also allow for more differentiated ice thickness estimations. For this reason, we attempted to use a remote sensing based lake dept estimation method proposed by Duguay and Lafleur (2003), but did not succeed (see Section 5.2). While we could show that the method would theoretically also work with Sentinel-2 Surface Reflectance (SR) products in Churchill (which is where Duguay and Lafleur (2003) had previously tested their method), we could neither reproduce the same results in Barrow nor in Kytalyk, as the method appears to be highly dependent on water purity (transparency). A fact they acknowledged in their publication. In Kytalyk and in Barrow, most of lakes were very *dirty* (see Figure 5.9), which led to measuring the reflectance of the suspended particles instead of the lakebed translucing through the water. This effect worsens with increasing lake depth, which therefore affected the Kytalyk site the most, as, judging by both the high backscatter intensity of floating ice (see Section 5.1) and the overall scarce occurrence of grounded ice despite very low temperatures (see Section 5.4), the lakes are generally deeper compared to both Barrow and Churchill. Even for more shallow lakes, we have to assume that it would be rather difficult to post-correct for water impurities, as the concentration of suspended particles in the lakes can vary strongly, both temporally, as well as spatially. For these reasons, we have to conclude, that this method is unsuitable for assessing lake depths consistently across multiple study sites. Also, to date, no bathymetric datasets are available on GEE that do not exclusively include ocean floors. This lack of widely accessible and frequently updated information on lake bathymetries is presumably one of the major limitations on advancing our understanding of the relationship between climate and subarctic lake ice regimes on a larger scale. Studies on grounded ice would greatly benefit from further development and implementations of remote sensing based methods of assessing lake depth.

6.2 VV vs. HH-pol based classifications

In Section 5.3 and 5.4 we found, that both VV and HH polarised Sentinel-1 scenes worked well for grounded ice detection at both primary study sites using the same thresholding method (see Section 4.5). Given that both co-pol variants have been successfully used for grounded ice detection in the past, this conformed to our expectations. There are however distinct differences between both polarisations. When comparing the the two co-polarised γ_E^0 backscatter frequency distributions of the Barrow lakes, γ_E^0 backscatter values in the HH-polarised EW scenes were generally higher. HH-frequencies of the floating ice class within our 4 years study period peak around an average of -8.0 dB in the frequency distributions. The VV-polarised IW scenes on the other hand have their average frequency maximum around -10.7 dB, which is 2.7 dB lower. In Kytalyk, the difference of the average of the most frequently occurring pixel brightness value is very similar with 2.5 dB, but the values are generally much higher (-4.1 dB HH, -6.6 dB VV), indicating a thicker floating ice cover. Consequently, the determined threshold for our HH-pol based classifications is also higher compared to threshold of the the VV-pol based ones (see Figure 4.2). This must be due to HH polarised SAR pulses being generally more sensitive to vertical corner reflection - the main scattering component of floating ice (Duguay et al., 2002) - compared to VV polarised waves. For the masked Barrow scene, both polarisations show a distinct bi-modality with approximate Gaussian distributions in the image histograms (see Section 4.9). However, the HH-polarised images on average actually show consistently a greater separation distance between the two maxima (8.3 dB) compared to the VV-polarised ones (7.0 dB). This leads to the 4 years average HH-pol pixel count of the local minimum (0.1 dB bucket width) being only 32.4% of that of the corresponding floating ice maximum, while for VV-polarisation, this number is with 66.5% much higher (see example in Figure 6.1).

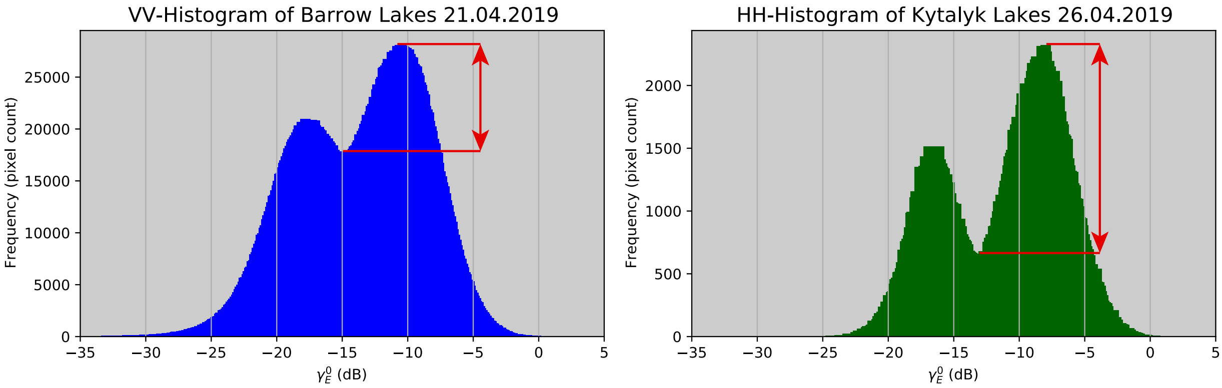

FIGURE 6.1: VV- (left) and HH-polarised (right) frequency distributions of the Barrow lake ice backscatter during state of ice maximum. The bi-modality is well visible using both polarisations, however, better separation of the two classes (grounded and floating ice) can be achieved with HH polarised images, as the *valley* between the two approximate Gaussian curves is much deeper for HH compared to VV-polarisation (red arrows).

Consequently this means that when using HH-polarisation, there are less pixels whose backscatter values are very close to the threshold. Close to threshold pixels are more ambiguous to assign to either the floating or the grounded ice class. In short, this means that HH would generally be the preferable polarisation over VV to use for grounded ice detection, especially if we opted to produce accurate maps. Unfortunately, the Sentinel-1 observation scenario is designed in such a way, that HH polarised data over sea-adjacent subarctic regions is only acquired in the spatially and temporally less detailed, geographically more limiting (does not go far inland) and generally more noisy EW format (Miranda et al., 2017). This data situation is not optimal for grounded ice detection and therefore compromises need to be made. For the purpose of lake ice classification, HH-polarised IW mode would certainly be the most desirable combination. But as we have shown in Section 6.2 and 5.4, if we mainly opt to just detect the general magnitude and relative changes between years of the grounded ice formation, using VV-pol based classifications instead seems to work just as well. We need to make clear that because we had neither ground truth nor model calculations directly available for this study, we unfortunately can not provide any hard numbers on accuracy for any of our classifications. Using the Duguay and Wang (2018) dataset as a proxy, we can assume that the HH-based classifications would generally be more accurate (see Section

5.6). However, because they probably have used the same HH-pol EW swath for their comparison with the model calculation as we did, there is a bias in favour of our HH-based classification. Those results therefore need to be taken with caution. We have also seen in Section 5.3, that VV-based classifications always gave us higher numbers for grounded ice compared to HH and that this effect increased with higher fractions of grounded ice. This discrepancy between VV and HH-pol gronded ice percentages is however largely systematic, and can be calculated by using factor 0.9. This peculiar circumstance could potentially be very useful to fill in gaps in historical grounded ice time series using differently polarised images. However, further investigation into the matter would be necessary to explain why this discrepancy happens and whether the 0.9 factor is Sentinel-1 sensor specific or acquisition mode dependent or if it would also work for entirely different sensors. Also, more statistical support would be needed, before this particular relationship could be firmly postulated.

6.3 Cross polarisations: Useful or useless?

As we have seen in Section 5.5, using cross polarisations to detect grounded ice did not produce very useful results. This has certainly to do with backscatter values and therefore also our thresholds overall being very low (especially HV, with a threshold of -26.9 dB), which is problematic, as it is close to the NESZ noise floor (Miranda et al., 2017). This surprised us, as based on the stratigrahic ice diagrams produced by Duguay et al. (2002), we were expecting volume scattering to play a more important role among the backscatter mechanisms of floating ice. The larger problem however, was the bad separability of the two ice classes based on the cross-pol image histograms. Apparently, the backscatter changes more gradually between floating and grounded ice in cross-pol, which leads to nearly no visible bi-modality in the frequency distribution of the images. The thresholding process was then further complicated by some sorts of calibration changes (especially visible in VH-pol) that seem to have happened within our 4 years observation period. We therefore had to basically guess where we suspected that one class ends and the other one starts in the histograms, which led to potentially quite bad threshold placements. This is especially visible in the VH-polarisation, where the resulting grounded ice fractions did not remotely match the co-pol based ones (see Figure 5.11), because the threshold was set too high (-22.8 dB). Combined with the NESZ problem, this is certainly an issue. We could therefore just conclude that cross-polarisations are useless for the purpose of grounded ice detection. However, we think that it would be too early for that: While we have examined all four polarisation modes separately, we have completely ignored the possibility of combining them together. The benefits of the VV+VH and HH+HV polarisation modes of Sentinel-1 after all, is the possibility to analyse fully polarised backscatter from the vertically or horizontally polarised pulses. For future grounded ice mapping studies, it could therefore be very interesting to analyse, whether including the cross-polarised band into the corresponding co-polarised classification would improve the accuracy of the results. Additionally, combining co- and cross-pol would allow for setting the threshold in a 2-dimensional frequency distribution space, which could potentially lead to cleaner separation of the two classes. Considering however the calibration issues of the Sentinel-1 cross-pol channels, we have our doubts whether a combination would be beneficial, using a fixed threshold for all scenes, at this point in time.

6.4 Strengths and weaknesses of our Methods

The basic concept behind this work was, to keep the workflow and methods of our ice regime mapping relatively simple compared to what some previous studies did (Arp et al., 2011; Antonova et al., 2016; Surdu et al., 2016) We also restricted ourselves to using data that is freely available on GEE, in mind that even non-experts in this field could relatively easily follow our methods and create their own grounded ice maps for other subarctic lake areas. We think that this goal was only partially reached. While our methods worked well for us, we acknowledge that they have weaknesses, that need to be discussed.

Our threshold determination method relies on clearly visible bi-modality in the frequency distribution of the masked lake ice backscatter. As we have seen in Section 4.5 this can be very problematic for study areas that form very little grounded ice, such as Kytalyk. Because of this, we were unable to determine our classes directly from the Kytalyk scenes, but we had to adopt the threshold from the Barrow site instead. We ended up demonstrating that a threshold, which was determined on the basis of one study (Barrow) site, can be smoothly carried over to a different one (Kytalyk) as long as we are using the same sensor type and acquisition mode. Howeverm this undermined our original intent for our threshold-determination method to work the same regardless of the study site. Furthermore, manual minimum and maximum determination requires a lot of user input and can therefore be quite laborious, especially if we are looking at a long period of time with more images and therefore more histograms to analyse. More importantly, the exact values of the local minimum that we used in order to set the threshold is not only dependent on bucket size, but also on residual image noise, and therefore does not necessarily accurately reflect the exact point of division between grounded and floating ice. These problems could be mitigated by using statistical data processing in order to split the two classes, as it was done by Engram et al. (2018). They used an algorithm they adopted from Ajadi et al. (2016), to find the best fit of two Gaussian curves in their image histograms, and then set the threshold at the intersection point of the two curves, resulting in an equal-error, unbiased threshold for each image. With this method, it would have been easily possible to determine a threshold from the co-polarised Kytalyk scenes. But on the other hand, this method is also not exactly simple and laymen friendly. About thresholding, it also needs to be said that when the ice starts to ground, it goes through a transitional period where backscatter values are close to our threshold values. As we have discussed in Section (6.2), the backscatter drop seems to happen more gradually in the VV-polarisation than in the HH-polarisation, leading to less separation between the two classes. But regardless of the utilized polarisation mode, there is a certain range of backscatter values where the physical basis for the classification is not very clear at all and argumentative cases could be made for setting the threshold either higher or lower from the Gaussian curve intersection. In short, due to the transition between the ice classes being gradual, a certain degree of ambiguity at the transition point is unavoidable.

One of the challenges we faced in this work was to find some points of reference in order to get some idea on whether our resulting maps would be plausible. As we had neither ground truth nor ice model calculations available, our possibilities were limited. The Duguay and Wang (2018) dataset came in handy for that, as we could assess whether our method would produce maps that were more or less spatially accurate results. However, their dataset did not cover the whole time frame we wanted to examine and was therefore only usable for assessing whether our thresholding method would work in principle or not (as we explained in Section 5.6). However, in order to be able to answer our third research question (see Chapter 1), we needed some reference that covered the whole 4 years time period. For this, we used the ECMWF ERA5 climate reanalysis dataset. Relatively early on, we had decided, that we wanted to boil down our time series to one scene (per polarisation) for each year. It was therefore very important that we selected the scenes with the maximum ice thickness per year, as otherwise we could not expect to see a clear correlation with the ERA5 climate indicators. Our approach to do this included a manual selection of lakes representing different ice regime compositions (see Section 4.4). This method turned out to be quite cumbersome. We had to make sure that for every year we had some lakes in our selection that started to ground very late, in order to not select a scene that was too early in the winter. This would have resulted in classifications under-representing the proportion of grounded ice. To do this, it was necessary to iterate the selection process multiple times while checking our timeseries backscatter graphs (see Figures 5.3 and 5.5) until we had late-grounding lakes selected for each year. For this work, we only selected 6 lakes, in order to produce well arranged and easy to discuss figures. However, it would certainly be better to select more lakes than that, to gain higher certainty regarding the determined ice maxima. It is therefore clear, that this method requires a lot of user involvement, also because the selected lakes need to be categorised into the *always-non-grounding* and *(partially) grounding* groups afterwards. The selected Sentinel-1 scenes to represent the ice-maximum, were all temporally located towards the end of the seasons, before temperatures went over 0°C. Because our method put weight on peak backscatter brightness of non-grounding lakes, it is robust against accidentally giving us a resulting ice-maximum that would be too late in the season, and fall into the melting period. Other works (Duguay and Wang, 2019; Surdu et al., 2016) usually did the thresholding and classification for multiple SAR scenes per season and then identified the image showing the maximum ice thickness from the resulting grounded ice fractions. This method might have been less laborious, however it also poses a higher risk to select a scene that is too late in the season, as melting floating ice could be misidentified as grounded ice (Morris et al., 1995). As we could see in Section 5.4, our results appeared to correlate relatively well with the ERA5 climate indicators and therefore, we can assume that our scene selection was quite good. Interestingly though, the relatively large acquisition time difference between the 2018 IW and EW scenes in Kytalyk (see Table 4.1) was hardly noticeable when comparing the VV and HH based classifications (see Table 5.2). It therefore seems that, as long as we do not select a scene that is too late or way too early, the selection of the ice-maximum-scene is not (always) as highly critical for the climate correlation to be visible, as we originally assumed. Of course one should keep in mind, that the perfect moment of the maximum lake-ice mass cannot be found anyway, given that we have to work with a 12 days temporal resolution. Our determined yearly grounded ice fractions are therefore always remaining approximations. That being said, devising an automation of the ice-maximum-scene selection process would certainly be worthwhile for future studies.

As we have already mentioned in Section 4.3, our approach for lake masking was to minimise the likelihood of having pixels falsely classified as water. This led to a slight underestimation of grounded ice using our lake mask compared to the one used by Duguay and Wang (2018), as mentioned in Section 5.6. While this was hardly an issue for us when looking at a timeseries of only 4 years, this could pose a bigger problem when observing longer time-spans, as the probability of more significant changes in the hydrology rises (Grosse et al., 2013). Due to the melting of permafrost, newly formed lakes as well as ponds that drained during the study time period would simply be ignored in the resulting lake ice maps. Because of this, updating lake masks between winters could improve the results and ice regime classification timeseries could safely be extended further into the future. A combination of SAR based lake ice classifications with SAR based flood mapping, such as the approach proposed by Twele et al. (2016), would therefore be viable to look into in future studies.

7 Conclusions

As we have now discussed our results, we now draw our conclusions, first by addressing our research questions:

1. How well can we map grounded ice in Kytalyk and Barrow with Sentinel-1 and other data freely accessible in GEE?

When we analysed the Sentinel-1 IW VV-pol based continuous time series of the thermokarst lakes for the years 2017 to 2020, the typical annual April-May backscatter drops associated with the grounding of the ice was clearly detectable at both study sites. Using the temporal VV-backscatter profile of the lakes, we were able to identify a date for each year (with a temporal resolution of 12 days), where lake ice thickness must have been at its maximum, therefore reducing the timeseries to 1 image per year, site and polarisation mode. We then proceeded to classify the lake ice, using the bi-modality of the frequency distribution of the lake ice surfaces to set one fixed threshold backscatter value for all four years and both study sites per polarisation. Annual changes in both co-pol based classifications appeared to correlate well with ECMWF ERA5 climate indicators. An additional comparison of our EW HH-based with the also Sentinel-1 EW HH-pol based Duguay and Wang (2018) dataset (92.56% accuracy to model calculations), yielded overall great consistencies of 97.01% (Barrow) and 97.59% (Kytalyk). However, our HH classifications consistently overestimated grounded ice fractions by about 2.5%, indicating that our threshold might have been set slightly too high.

GEE grants access to multiple very useful datasets for grounded ice mapping, such as the JRC Global Surface Water datasets which were very useful for lake masking purposes and the ECMWF ERA5 climate reanalysis product. All the necessary calculations, including the radiometric recalibration of the Sentinel-1 scenes from σ^0 to γ_E^0 could easily be accomplished in GEE. We therefore conclude, that GEE is very useful for the purpose of subarctic ice regime classification.

2. How well do different polarisations work for classifying lake ice?

Our analysis confirmed, that grounded and floating ice are well discriminable with both VV and HH polarisations. However HH allows for a slightly better statistical separation between the two classes because of less overlap in the bi-modal frequency distribution. Using the same thresholding method for both polarisations, classifications based on EW HH-pol showed consistently less grounded ice over both study sites compared to IW VV-pol. This deviation has a strong systematic component, as VV-detected grounded ice fractions could be approximated by multiplying HH-grounded ice percentages by 0.9. Nevertheless, consistencies between the co-pol based classification always remained above 90% in all of our tests.

Our cross-pol (VH and HV) based results, however, are less promising. Not only was there no clear bi-modality visible in their frequency distributions, which complicated the thresholding process, but their results were also relatively inconsistent to each other, with overall consistencies of all tests in Barrow being below 90%. Additionally, the annual changes of the cross-pol derived grounded ice percentages often disagreed with the ones based on co-pol (e.g. grounded ice increased in co-pol while it decreased in cross-pol). Furthermore, thresholds would have to be set very low (-26.9 dB for HV) in order to come close to the results of the co-pol classifications, which is arguably too close to the noise floor of the Senitinel-1 sensors.

3. How well can we detect temporal changes in grounded ice formation between 2017 and 2020?

Using the co-polarised images, we detected quite substantial variations in the grounded ice extent over the four years period from 2017 to 2020 at both study sites. In Barrow, the grounded ice fraction rose over the four years time span from 35.42% (VV)/32.53% (HH) to 48.48% (VV)/44.21% (HH). Our climate-correlation analysis using ECMWF ERA5 data showed, that this increase was largely caused by a drop in average winter temperature of more than 2°C and simultaneously an increase in wind speed leading to less thick snow-cover. In Kytalyk, grounded ice fractions rose from 5.99% (VV)/5.61% (HH) in 2017 to more than double, 13.92% (VV)/12.29% (HH) in 2019 followed by a smaller decrease again to 10.59% (VV)/9.52% (HH). This could be explained by a strong decrease in average winter temperature from 2017 to 2019 by nearly 2.5°C, followed by a only slightly warmer winter in 2020, though with substantially more snow.

While these results from our analysis are positive, we were unable to fully explain the magnitude of the changes, for the following two reasons: 1. In our climate correlation analysis, we only considered three factors, namely average temperature, snowfall and wind speed and ignored their temporal variations as well as other factors. Our analysis was highly interpretative, and the climate factors were not weighted. 2. As we were both unable to either directly acquire bathymetric data in GEE or derive it from optical sensors (Sentinel-2, Landsat 8), it was not possible to infer ice thickness from our classification maps and therefore there was a critical link missing in our analysis.

4. What are differences in grounded ice formation between Kytalyk and Barrow?

Despite mean winter temperatures in Kytalyk being more than 5°C lower than in Barrow, detected grounded ice fractions were substantially lower, never exceeding 14% compared to Barrow where in 2020 the grounded ice fraction proportion approached 50%. Floating ice backscatter in Kytalyk can get much brighter than in Barrow, pointing to a thicker ice layer caused by the lower temperatures. From these findings, we have to conclude that, on average, the lakes in Kytalyk must be substantially deeper (potentially multiple meters) than in Barrow, making the occurrence of grounded ice much rarer. This circumstance was also the main reason, why we were unable to find grounded ice in Kytalyk in our previous study (see Appendix).

In addition to answering our research questions, we can also state the following:

While our methods ended up working well within the framework of this thesis as we were able to use the same thresholds for Kytalyk that we derived from the Barrow site, our thresholding method is problematic for sites with small fractions of grounded ice. In such cases, without adopting, setting the threshold would either rely on excessive eyeballing, or require more sophisticated statistical analysis tools, undermining the aspired simplicity of our methods. Given the fact that our thresholds are only based on a very small sample size and only one study site, we would not recommend for further studies to just adopt our threshold values.

Further studies with access to either ground truth or model calculations would be needed, to determine the more precise accuracies of the different polarisation based classifications. Also, we were unable to explain the systematic deviations between the EW HH and the IW VV based maps within the framework of this study. In order to potentially leverage the implications of this conjecture, further investigation and statistical analysis would certainly be necessary. Additionally, even though on its own cross-pol did not fare well in grounded ice mapping, we think that a combination of co-pol with its corresponding cross-pol would be worth investigating in this context. Lastly, we think that the current lack of widely available bathymetric data concerning mid-to-small sized lakes is one of the major current limitations for further advancements of our understanding of the freezing processes of these lakes and subsequently their CO_2 and methane exchange on a global scale. We therefore believe that the creation of a frequently updated global bathymetric lake dataset would be worth the effort involved in such an undertaking.

Bibliography

Ajadi, O. A., F. J. Meyer, and P. W. Webley (June 2016). “Change Detection in Synthetic Aperture Radar Images Using a Multiscale-Driven Approach.” *Remote Sensing* 8.6, p. 482.

Anthony, K. M. W., S. A. Zimov, G. Grosse, M. C. Jones, P. M. Anthony, F. S. C. Iii, J. C. Finlay, M. C. Mack, S. Davydov, P. Frenzel, and S. Frolking (July 2014). “A shift of thermokarst lakes from carbon sources to sinks during the Holocene epoch.” *Nature* 511.7510, pp. 452–456.

Antonova, S., C. Duguay, A. Kääb, B. Heim, S. Westermann, M. Langer, and J. Boike (2016). “Monitoring bedfast ice in lakes of the Lena River Delta using TerraSAR-X backscatter and coherence time series.” *EPIC3XI. International Conference on Permafrost*. Potsdam, Germany.

Arp, C. D., B. M. Jones, F. E. Urban, and G. Grosse (July 2011). “Hydrogeomorphic processes of thermokarst lakes with grounded-ice and floating-ice regimes on the Arctic coastal plain, Alaska.” *Hydrological Processes* 25.15, pp. 2422–2438.

Drusch, M., U. Del Bello, S. Carlier, O. Colin, V. Fernandez, F. Gascon, B. Hoersch, C. Isola, P. Laberinti, P. Martimort, A. Meygret, F. Spoto, O. Sy, F. Marchese, and P. Bargellini (May 2012). “Sentinel-2: ESA’s Optical High-Resolution Mission for GMES Operational Services.” *Remote Sensing of Environment* 120, pp. 25–36.

Duguay, C. R. and P. M. Lafleur (Jan. 2003). “Determining depth and ice thickness of shallow sub-Arctic lakes using space-borne optical and SAR data.” *International Journal of Remote Sensing* 24.3, pp. 475–489.

Duguay, C. and J. Wang (July 2019). “Advancement in Bedfast Lake ICE Mapping From Sentinel-1 Sar Data.” *IGARSS 2019 - 2019 IEEE International Geoscience and Remote Sensing Symposium*. Yokohama, Japan: IEEE, pp. 6922–6925.

Duguay, C. R., T. J. Pultz, P. M. Lafleur, and D. Drai (June 2002). “RADARSAT backscatter characteristics of ice growing on shallow sub-Arctic lakes, Churchill, Manitoba, Canada.” *Hydrological Processes* 16.8, pp. 1631–1644.

Duguay, C. R. and J. Wang (2018). *Lake Ice Classification from Sentinel-1A 2015 - 2018*. Type: data set. URL: `https://doi.org/10.1594/PANGAEA.889727`.

Engram, M, K. W. Anthony, F. J. Meyer, and G Grosse (2013). “Characterization of L-band synthetic aperture radar (SAR) backscatter from floating and grounded thermokarst lake ice in Arctic Alaska.” *The Cryosphere*, p. 12.

Engram, M., C. D. Arp, B. M. Jones, O. A. Ajadi, and F. J. Meyer (May 2018). “Analyzing floating and bedfast lake ice regimes across Arctic Alaska using 25 years of space-borne SAR imagery.” *Remote Sensing of Environment* 209, pp. 660–676.

Feng, M., C. Huang, S. Channan, E. F. Vermote, J. G. Masek, and J. R. Townshend (Jan. 2012). "Quality assessment of Landsat surface reflectance products using MODIS data." *Computers & Geosciences* 38.1, pp. 9–22.

Filipponi, F. (2019). "Sentinel-1 GRD Preprocessing Workflow." *Proceedings* 18.1, p. 11.

Gorelick, N., M. Hancher, M. Dixon, S. Ilyushchenko, D. Thau, and R. Moore (Dec. 2017). "Google Earth Engine: Planetary-scale geospatial analysis for everyone." *Remote Sensing of Environment* 202, pp. 18–27.

Grosse, G., B. M. Jones, and C. D. Arp (2013). *Thermokarst lakes, drainage, and drained basins*. Vol. 8. Pages: 325-353.

Hersbach, H., B. Bell, P. Berrisford, S. Hirahara, A. Horányi, J. Muñoz-Sabater, J. Nicolas, C. Peubey, R. Radu, D. Schepers, A. Simmons, C. Soci, S. Abdalla, X. Abellan, G. Balsamo, P. Bechtold, G. Biavati, J. Bidlot, M. Bonavita, G. Chiara, P. Dahlgren, D. Dee, M. Diamantakis, R. Dragani, J. Flemming, R. Forbes, M. Fuentes, A. Geer, L. Haimberger, S. Healy, R. J. Hogan, E. Hólm, M. Janisková, S. Keeley, P. Laloyaux, P. Lopez, C. Lupu, G. Radnoti, P. Rosnay, I. Rozum, F. Vamborg, S. Villaume, and J. Thépaut (July 2020). "The ERA5 global reanalysis." *Quarterly Journal of the Royal Meteorological Society* 146.730, pp. 1999–2049.

International Cooperation Copernicus (2021). URL: `https://www.copernicus.eu/en/about-copernicus/international-cooperation` (visited on 01/14/2021).

Jeffries, M. O., K. Morris, and G. E. Liston (1996). "A Method to Determine Lake Depth and Water Availability on the North Slope of Alaska With Spaceborne Imaging Radar and Numerical Ice Growth Modelling." *Arctic* 49.4, pp. 367–374.

Jeffries, M. O., H Wakabayashi, and W. F. Weeks (1993). "ERS-1 SAR backscatter changes associated with ice growing on shallow lakes in arctic Alaska." *Proceedings of IGARSS '93 - IEEE International Geoscience and Remote Sensing Symposium* 4, pp. 2001–2004.

Jones, B. M., A. Gusmeroli, C. D. Arp, T. Strozzi, G. Grosse, B. V. Gaglioti, and M. S. Whitman (Dec. 2013). "Classification of freshwater ice conditions on the Alaskan Arctic Coastal Plain using ground penetrating radar and TerraSAR-X satellite data." *International Journal of Remote Sensing* 34.23, pp. 8267–8279.

Klerk, P. de, A. Teltewskoi, M. Theuerkauf, and H. Joosten (2014). "Vegetation patterns, pollen deposition and distribution of non-pollen palynomorphs in an ice-wedge polygon near Kytalyk (NE Siberia), with some remarks on Arctic pollen morphology." *Polar Biol* 37, pp. 1393–1412.

Knight, E. and G. Kvaran (Oct. 2014). "Landsat-8 Operational Land Imager Design, Characterization and Performance." *Remote Sensing* 6.11, pp. 10286–10305.

Kokelj, S. V. and M. T. Jorgenson (2013). "Advances in Thermokarst Research." *Permafrost and Periglacial Processes* 24.2, pp. 108–119.

Louis, J., V. Debaecker, B. Pflug, M. Main-Knorn, J. Bieniarz, U. Mueller-Wilm, E. Cadau, and F. Gascon (Aug. 2016). "SENTINEL-2 SEN2COR: L2A Processor for Users." *Proceedings Living Planet Symposium 2016*. Vol. SP-740. Prague, Czech Republic: Spacebooks Online, pp. 1–8.

Loveland, T. R. and J. L. Dwyer (July 2012). "Landsat: Building a strong future." *Remote Sensing of Environment*. Landsat Legacy Special Issue 122, pp. 22–29.

Miranda, N., P. Meadows, R. Piantanida, A. Recchia, D. Small, A. Schubert, P. Vincent, D. Geudtner, I. Navas-Traver, and F. C. Vega (July 2017). "The Sentinel-1 constellation mission performance." *2017 IEEE International Geoscience and Remote Sensing Symposium (IGARSS)*, pp. 5541–5544.

Morris, K., M. O. Jeffries, and W. F. Weeks (Apr. 1995). "Ice processes and growth history on Arctic and sub-Arctic lakes using ERS-1 SAR data." *Polar Record* 31.177, pp. 115–128.

Muster, S., K. O. Roth, M. Langer, S. Lange, F. Cresto Aleina, A. Bartsch, A. Morgenstern, G. Grosse, B. Jones, A. B. K. O. Sannel, Y. O. Sjoberg, F. O. Gunther, C. Andresen, A. Veremeeva, P. R. Lindgren, F. Bouchard, M. J. Lara, D. O. Fortier, S. O. Charbonneau, T. A. Virtanen, G. Hugelius, J. Palmtag, M. B. Siewert, W. J. Riley, C. D. O. Koven, and J. O. Boike (June 2017). "PeRL: a circum-Arctic Permafrost Region Pond and Lake database." *Earth System Science Data (Online)* 9.1.

Olivas, P. C., S. F. Oberbauer, C. E. Tweedie, W. C. Oechel, and A. Kuchy (Dec. 2010). "Responses of CO $_2$ flux components of Alaskan Coastal Plain tundra to shifts in water table." *Journal of Geophysical Research* 115, G00I05.

Pekel, J.-F., A. Cottam, N. Gorelick, and A. S. Belward (Dec. 2016). "High-resolution mapping of global surface water and its long-term changes." *Nature* 540.7633, pp. 418–422.

Potin, M. P., M. B. Rosich, M. P. Grimont, M. N. Miranda, M. I. Shurmer, M. A. O'Connell, M. R. Torres, and M. M. Krassenburg (2016). "Sentinel-1 Mission Status." *11th European Conference on Synthetic Aperture Radar EUSAR 16*, pp. 59–64.

Potin, P., P. Bargellini, H. Laur, B. Rosich, and S. Schmuck (July 2012). "Sentinel-1 mission operations concept." *2012 IEEE International Geoscience and Remote Sensing Symposium*. Munich, Germany: IEEE, pp. 1745–1748.

Potin, P., B. Rosich, N. Miranda, P. Grimont, I. Shurmer, A. O'Connell, M. Krassenburg, and J.-B. Gratadour (July 2019). "Copernicus Sentinel-1 Constellation Mission Operations Status." *IGARSS 2019 - 2019 IEEE International Geoscience and Remote Sensing Symposium*. Yokohama, Japan: IEEE, pp. 5385–5388.

Siewert, M. B., J. Hanisch, N. Weiss, P. Kuhry, and G. Hugelius (Dec. 2014). "Total Storage and Landscape Partitioning of Soil Organic Carbon and Phytomass Carbon in Siberia." *AGU Fall Meeting Abstracts* 31, B31G–0107.

Surdu, C. M., C. R. Duguay, L. C. Brown, and D. Fernández Prieto (Jan. 2014). "Response of ice cover on shallow lakes of the North Slope of Alaska to contemporary climate conditions (1950–2011): radar remote-sensing and numerical modeling data analysis." *The Cryosphere* 8.1, pp. 167–180.

Surdu, C. M., C. R. Duguay, and D. Fernández Prieto (May 2016). "Evidence of recent changes in the ice regime of lakes in the Canadian High Arctic from spaceborne satellite observations." *The Cryosphere* 10.3, pp. 941–960.

Teltewskoi, A., F. Beermann, I. Beil, A. Bobrov, P. De Klerk, S. Lorenz, A. Lüder, D. Michaelis, and H. Joosten (Jan. 2016). "4000 Years of Changing Wetness in a Permafrost Polygon Peatland (Kytalyk, NE Siberia): A Comparative High-Resolution Multi-Proxy Study: Multi-Proxy Wetness Reconstruction of a Permafrost Polygon." *Permafrost and Periglacial Processes* 27.1, pp. 76–95.

Torres, R., S. Lokas, G. D. Cosimo, D. Geudtner, and D. Bibby (July 2017). "Sentinel 1 evolution: Sentinel-1C and -1D models." *2017 IEEE International Geoscience and Remote Sensing Symposium (IGARSS)*, pp. 5549–5550.

Twele, A., W. Cao, S. Plank, and S. Martinis (July 2016). "Sentinel-1-based flood mapping: a fully automated processing chain." *International Journal of Remote Sensing* 37.13, pp. 2990–3004.

Vermote, E., J. C. Roger, B. Franch, and S. Skakun (July 2018). "LaSRC (Land Surface Reflectance Code): Overview, application and validation using MODIS, VIIRS, LANDSAT and Sentinel 2 data's." *IGARSS 2018 - 2018 IEEE International Geoscience and Remote Sensing Symposium*, pp. 8173–8176.

Wakabayashi, H. and Y. Nishito (July 2015). "Monitoring of tundra lakes with C-band and L-band SAR data." *2015 IEEE International Geoscience and Remote Sensing Symposium (IGARSS)*, pp. 2076–2079.

Wakabayashi, H., W. F. Weeks, and M. O. Jeffries (Aug. 1993). "A C-band backscatter model for lake ice in Alaska." *Proceedings of IGARSS '93 - IEEE International Geoscience and Remote Sensing Symposium*. Vol. 3, pp. 1264–1266.

Walter, K. M., L. C. Smith, and F Stuart Chapin (July 2007). "Methane bubbling from northern lakes: present and future contributions to the global methane budget." *Philosophical Transactions of the Royal Society A: Mathematical, Physical and Engineering Sciences* 365.1856, pp. 1657–1676.

Wan, Z (Jan. 2008). "New refinements and validation of the MODIS Land-Surface Temperature/Emissivity products." *Remote Sensing of Environment* 112.1, pp. 59–74.

Wan, Z., Y. Zhang, Q. Zhang, and Z.-L. Li (Jan. 2004). "Quality assessment and validation of the MODIS global land surface temperature." *International Journal of Remote Sensing* 25.1, pp. 261–274.

Wulder, M. A., J. G. Masek, W. B. Cohen, T. R. Loveland, and C. E. Woodcock (July 2012). "Opening the archive: How free data has enabled the science and monitoring promise of Landsat." *Remote Sensing of Environment* 122, pp. 2–10.

Zimov, S. A. (Aug. 1997). "North Siberian Lakes: A Methane Source Fueled by Pleistocene Carbon." *Science* 277.5327, pp. 800–802.

Zona, D., D. A. Lipson, K. T. Paw U, S. F. Oberbauer, P. Olivas, B. Gioli, and W. C. Oechel (June 2012). "Increased CO2 loss from vegetated drained lake tundra ecosystems due to flooding." *Global Biogeochemical Cycles* 26, GB2004.

Zühlke, M., N. Fomferra, C. Brockmann, M. Peters, L. Veci, J. Malik, and P. Regner (Dec. 2015). "SNAP (Sentinel Application Platform) and the ESA Sentinel 3 Toolbox." *Sentinel-3 for Science Workshop, Proceedings of a workshop held 2-5 June, 2015 in Venice, Italy.*

GEO441 Remote Sensing Seminar, spring semester 2018

A Quest for Grounded Ice with Sentinel-1

Emanuel Vogel , Liv Fritsche , and Sebastian Hafner

Remote Sensing Laboratories, Department of Geography, University of Zurich

***Abstract*— The occurrence of floating and grounded ice has a crucial effect on the climate and is inversely influenced therefrom. Several studies have used space-born Synthetic Aperture Radar (SAR) to distinguish between liquid water, floating ice and grounded ice. Established literature associate the grounding of ice with a steep drop in backscatter due to changes in the dielectric contrast. This project examines said effect in a study site in Kytalyk, northern Siberia, with Sentinel-1 data. Although established methods have been applied and local conditions highly suggest the presence of grounded ice, the expected signature was not detected. This could either be due to an underestimation of the lake depths, indicating the need for higher resolved SAR data, or our approach was unsuitable for this site due to Sentinel-1 specific factors.**

I. INTRODUCTION

In sub-arctic regions thermokarst lakes are widespread. Most of them can be found in northern Siberia, Alaska and northern Canada. The development of these shallow lakes over time is in a strong correlation with the climate, as their occurrence is directly linked to the increasing thawing of permafrost in periglacial areas (Grosse et al. 2013). Fruthermore, the arctic and sub-arctic is not only strongly affected by global climate change, it also provides powerful positive feedbacks to further warming: Zimov et al. (1997) showed that thermokarst lakes are major sources of atmospheric methane, especially during the winter months when the lakes are frozen. The methane originates from Pleistocene sediments containing large amounts of carbon, previously conserved in the permafrost. Ice cover on these lakes does not prevent methane from leaking through pores in the ice. However, if the ice is grounded, the methane flux will be retained. Monitoring and estimating the proportion of floating to grounded ice of sub-arctic lakes can therefore be considered an important step to a better understanding and quantifying of the feedback-processes related to global warming (Muster et al. 2017). Due to the generally remote locations of thermokarst regions and the continuously dark winter months, space-borne Synthetic Aperture Radar (SAR) technology can be a valuable tool for observing these processes. Previous studies (Jeffries et al 1993, Wakabayashi et al. 2015) already succeeded in detecting and monitoring grounded ice in the northern-Alaskan thermokarst region Utqiavik, formerly known as Barrow, using relatively high-resolution fully polarimetric SAR data in X-, C- and L-band. For their detections, they took advantage of the microwave reflection properties of grounded lake ice, as described by Wakabayashi et al. (1993): When ice grounds, the backscatter intensity decreases drastically while floating ice appears very bright on the SAR images. The generally strong backscatter of floating ice can be explained by the ice-water interference causing a high dielecric contrast, coupled with the vertical geometry of trapped bubbles inside the ice acting as corner reflectors. For grounded ice, the soil under the ice absorbs the microwaves, as the dielectric properties of the soil and the ice are similar. (Antonova et al. 2016)

In this study, it was our goal to find out whether it is possible to detect and identify grounded ice in the tundra lakes of Kytalyk, north-eastern Siberia, using low-resolution Sentinel-1 8-days-extra-wide-swath composites. To our knowledge, no studies regarding grounded ice have yet been conducted in Kytalyk. One reason for this is certainly the hitherto poor coverage of the area in high-high resolution SAR images compared to Utqiavik. With the relatively recent launches of Sentinel-1A and B, C and D are planned, Kytalyk as well as other thermokarst areas will receive better temporal coverage than ever before. On top of that, Sentinel-1 data is completely free. If floating and grounded ice could indeed be distinguished in low-res Sentinel-1 data, this would strongly facilitate the monitoring of those regions and allow for the composition of low cost-time-series with sufficient data points.

II. STUDY SITE

Our study site (Figure 1) lies at around 71°N 147°E within the Kytalyk region in north-east Sakha, Russia. It is a sub-arctic thermokarst region, completely within thick, continuous permafrost. The mean annual temperature is around -14.5°C. Large parts of the landscape are affected by frequent flooding events of the rivers (most prominently Protoka Ularovskaya), resulting in an ever changing dynamic landscape. Another prominent feature are the innumerable thaw lakes which range in size from small pools to quite large lakes of around 100 km^2. These lakes are very dynamic as new lakes form from thawing of the permafrost while others drain. The riverbed in the lower right as well as in the upper right corner of the picture appears in a dark colour while lakes appear in different shades of green. For our study we concentrated on three middle sized lakes outside the flooding zones, where we could expect some consistency within the course of one year. The observed lakes are marked in Figure 1.

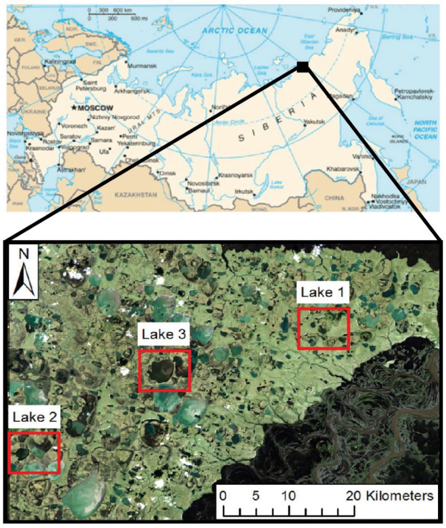

Fig. 1: Overview of the study site in Kytalyk (Siberia, Russia)

III. MATERIAL AND METHODS

A. *Temperature measurements*

The temperature measurements were acquired from the remotely sensed Land Surface Temperature (LST) product of the MODIS sensor. This freely available product is provided daily with a global coverage and a spatial resolution of 1 km (MOD11A1). The preprocessed LST was averaged over the entire study area and used for the interpretation of the SAR scenes.

B. *Optical imagery*

Landsat 8 Operational Land Imager (OLI) reflectance data, acquired between 25 July 2017 and 10 October 2017, was combined to a summer composite with minimal cloud cover and used to make a water mask of the study area. More specifically, a threshold was applied to a Modified Normalized Difference Water Index (MNDWI: Xu 2006) product, which was calculated with equation 1. The resulting mask has a spatial resolution of 40 m.

$$MNDWI = \frac{\rho_{Green} - \rho_{SWIR}}{\rho_{Green} + \rho_{SWIR}} \tag{1}$$

The bathymetry of the three lakes of interest was also mapped with optical data from the Landsat 8 OLI sensor. It was processed according to the approach presented by Duguay and Lafleur (2003) who classified the depth of shallow lakes and ponds in a sub-arctic region by relating Landsat Thematic Mapper (TM) Band 2 radiance $(Wm^2\mu m^{-1}sr^{-1})$ to lake depth (m), denoted in equation 2 as L and z, respectively. Duguay and Lafleur (2003) calibrated and tested their approach with in-situ measurements for lake depths ranging from 2 m to 8 m. Due to the deactivation of the TM mission in 2013, the mentioned data from Landsat 8, which measures green at a similar spectral range, was used in this study. Additionally, a relative depth scale was implemented due to the lack of ground truth in Kytalyk. The resulting map with a resolution of 30 m presents auxiliary information for the analysis of the SAR data.

$$z = 29.730e^{(-0.086L)} \tag{2}$$

C. *SAR scenes*

A total of 46 Sentinel-1 SAR composites were used for this study. The HH-polarized images were acquired in Extra Wide (EW) swath mode between the 3 July 2016 and 26 June 2017. This C-band acquisitions have a low resolution of 40 m. The EW mode has a swath width of 410 km and the incidence angle range is $18.9°$ to $47.0°$. A region growing algorithm developed by Kroon (2009) was applied to the water mask with seeds corresponding to the lakes illustrated in Figure 1. After isolating the three features in the SAR composites, statistical metrics of the backscatter for each of the acquired images were calculated. Thereafter, a time series showing the backscatter averaged over the whole lake (± standard deviation) and the corresponding averaged LST were plotted. Furthermore, critical time periods of the SAR scenes were chosen. The figures correspond to the marked extents illustrated in Figure 1 and visualize backscatter patterns and their intra-annual development.

IV. RESULTS

A. *Visual outputs*

In Figure 2, bathymetric maps and SAR scenes are visualized in three columns, showing Lake 1, Lake 2 and Lake 3 from left to right. The focus of this result section lies on these lakes. The scale of the lake depth ranges from deep to shallow, whereas deep indicates a depth of several meters and shallow a depth of less than a meter. According to the first row in Figure 2, Lake 1 is homogeneously not very deep with a particularly shallow, narrow area at the eastern water side. Lake 2 shows a dichotomy of a deeper part in the West and a more shallow eastern section. Lake 3 shows similar, although less pronounced traits than Lake 2, and additionally features a curved shallowness in the middle.

The first row of SAR scenes (A) represent the end of September when temperatures have already dropped well below 0°C. The backscatter is still fairly low on all three water bodies, especially on the smallest lake (Lake 1). An interesting pattern, which is featured on Lake 2 and Lake 3, are horizontal stripes of high backscatter intensities. On Lake 1, the southmost part shows a higher backscatter compared to its counterpart.

The following series of SAR scenes (B) were taken at the beginning of January during the coldest period of the year

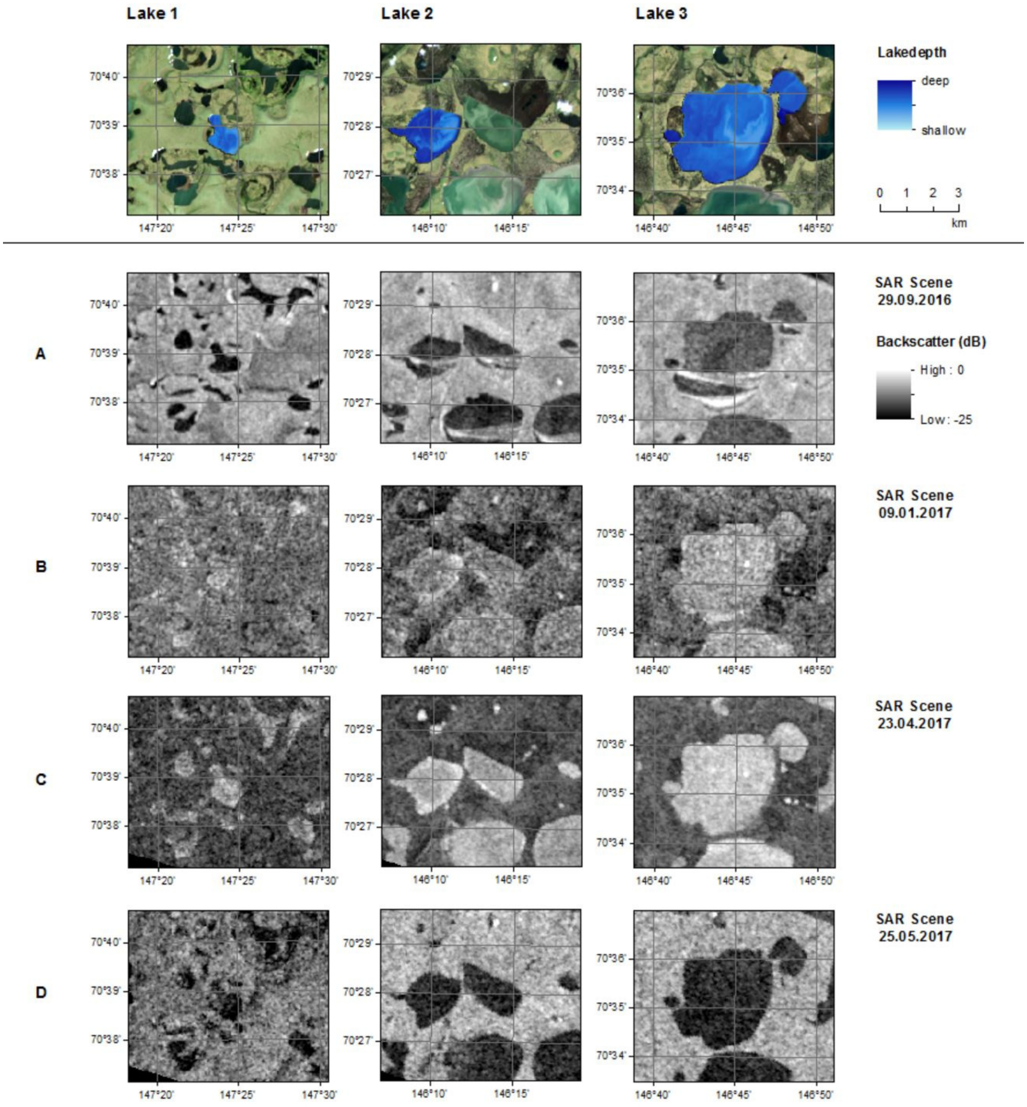

Fig. 2: Bathymetric maps and SAR scenes of Lake 1 (left), Lake 2 (middle) and Lake 3 (right)

with mean temperatures well below $-25°$C. Backscatters for all lakes are generally higher than on scene A (about -10 dB). They also all show small patches that are notably brighter than their surroundings. This patches are mostly concentrated along the land-water transition.

Row C shows the studied lakes towards the end of the winter season with rising temperatures which are still below the melting point. Compared to the previous scenes (B), all lakes appear brighter caused by an increased backscatter in the single digit range. The aforementioned brighter patches remain present. The larger lakes appear to be generally brighter than the smaller ones.

The last row (D) shows a temporal extent of the thawing season towards the end of May. Temperatures in that time of the year start to rise above $0°$C. All three observed lakes show a low backscatter intensity close to the minimum of -25 dB. Differences between all lakes are minimal.

B. Numeric time series

Time series showing the backscatter and temperature for the winter of 2016/2017 are illustrated in Figure 3. For all three lakes, a clear trend in increasing backscatter is visible starting at the end of September when temperatures drop permanently below $0°$, lasting until mid-March. This trend is followed by a stabilization of the backscatter intensities which starts once temperatures begin to rise again at the end of winter. After temperatures rise beyond the melting point, backscatters drop drastically for all studied lakes. The summer period is characterized by strong variations which differ between the lakes.

While the general trend in backscatter is similar, there are also some clear differences between the individual lakes. Lake 1, being the smallest of the studied water bodies has a backscatter intensity of about -7 dB during the aforementioned stable period. The largest lake (Lake 3) and the mid-sized lake (Lake 2) both have a higher peak of about -4 dB and -5 dB, respectively. Another difference is that the backscatter of Lake 1 is slightly more heterogeneous during summer compared to the larger lakes, indicated by a higher standard deviation. Additionally, Lake 1 shows a decidedly smoother decrease in backscatter in the thawing season, while the other two lakes show a much steeper drop. This sudden decrease in backscatter is preceded by a clear seasonal peak in signal strength. On the other hand, this feature is absent in the data of Lake 1.

V. DISCUSSION

A. Prerequisites for grounded ice

The results of the bathymetric estimates suggest that the depths of all three studied lakes lie in the range of single-digit meters. However, our bathymetric estimates show some irregularities. For example in Lake 2, a relatively slim strip at the right shore appears to be much deeper than most of the lake, which in fact is rather improbable considering the geomorphological history of this landscape. The other lakes show very similar irregularities: Most of them appear to be deeper at the land-water transition than at the center. These observed phenomena might be artefacts of water impurities coupled with turbulences. It must also be said that these depths are not calibrated with in-situ measurements from Kytalyk, as we were not able to visit the site within the boundary of this study. Despite these possible sources of errors and inaccuracies, the bathymetric maps indicate that the lakes in our region of interest are generally shallow, which is a characteristic attribute of sub-arctic lakes and ponds. Amongst others, those attributes are also described in Duguay and Lafleur (2003) who were able to observe grounded ice in abundance at their study site in northern-Alaska. Given those circumstances coupled with the fact that the temperatures of the winter months of 2016/2017 provided by MODIS lie consistently below $-25°$C, the existence of grounded ice is highly expected in small and mid-sized lakes

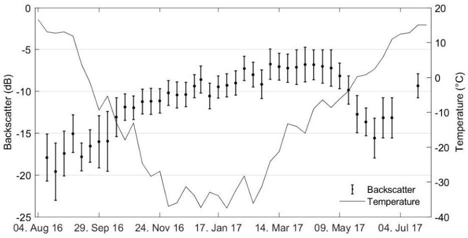

(a) Lake 1

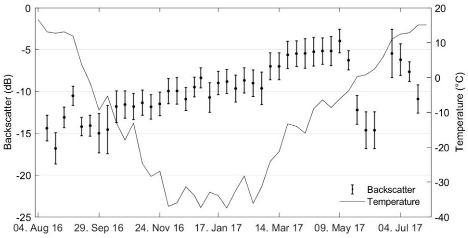

(b) Lake 2

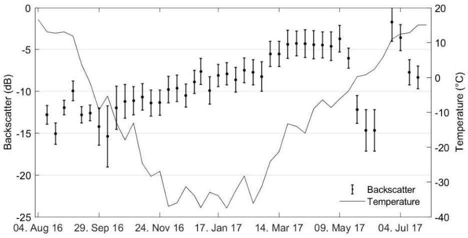

(c) Lake 3

Fig. 3: Backscatter and temperature time series of the study lakes

in our study site.

B. Interpretation of SAR observation

Generally, low backscatter is characteristic for relatively smooth water surfaces, as the microwaves are mostly scattered away from the sensor. However, wind conditions influence surface roughness due to the formation of waves, causing high temporal variation during summer months. This effect can be seen in all timeseries visualized in Figure 3. Once water starts to freeze, growing ice thickness causes an increasing backscatter (Wakabayashi et al. 1993). This is well visible on both, the visual SAR scenes as well as the time series from September to April. During the thawing season at the end of winter, the strong drop in backscatter can be traced back to the effect of melting ice on signal intensity described in Dugay and Lafleur (2003). This overall sequence in backscatter evolution is completely in line with the literature for floating ice.

Based on the prerequisites for grounded ice, however, we expected a drop of several dB in backscatter within a relatively small timeframe within our data. This drop is associated with grounding ice as reported, amongst others, by Jeffries et al. (1993), Duguay and Lafleur (2003), Atwood et al. (2015), Wakabayashi et al. (2015) and Antonova et al. (2016). This phenomenon is completely absent in our data even though grounded ice is highly expected in the study site as mentioned in the previous subsection. Particularly the absence of the grounding ice signature at the borders of the lakes is unexpected due to the fact that those areas are necessarily shallow. Based on the temperature condition on site, the ice should be of sufficient thickness to reach the ground there. However, neither the standard deviation in the time series, nor the visual outputs suggest the presence of grounded ice at the borders.

C. Potential causes of discrepancy

In consideration of our core assumption regarding the landscape of Kytalyk, the absence of the grounded ice signature is in substantial conflict with the established literature. Thus, potential factors influencing our results had to be thoroughly analyzed to find the source of this discrepancy, taking into account comparable papers on this issue. A very recent study addressing this topic by Engram et al. (2018) shows that the signature of grounded ice varies temporally as well as between sensors. This finding has to be taken into account because it additionally complicates the detection of grounded ice without in-field calibration. The following factors were identified to be the most probable ones for the discrepancy:

1) Resolution: The low spatial resolution of 40 m of the Sentinel-1 SAR data could be a crucial factor for the missing grounded ice signature at the border of the lakes. Antonova et al. (2016) and Engram et al. (2018) have successfully detected grounded ice using very high to high resolution SAR imagery (10 m and 12.5 m). The low resolution of our data, however, is likely to obscure small grounded ice patches by mixing this feature with the backscatter of adjacent areas. This, however, would mean that the border effect of grounded ice is very narrow and that the lakedepth is consequently underestimated in our approach. Given that abovementioned assumptions are true, our approach could lead to a successful detection of grounded ice for more shallow lakes in comparable climatic environments. This assumption is supported by the fact that Duguay and Lafleur (2003) and Jeffries et al. (1993) successfully detected grounded ice with a resolution of 30 m and 100 m respectively.

2) Incidence angle: Another factor which could influence the backscatter is the incidence angle. Although SAR images are corrected for this effect, the incidence angle correction might not be able to account for the angle-dependent differences in microwave-surface interaction. Nevertheless, none of the beforementioned papers expressed concern about the effects of different incidence angles on the detection of grounded ice.

3) other factors: As the C-Band has been proven to be a viable frequency for the distinction between floating and grounded ice by several other studies (e.g. Jeffries et al. 1993, Duguay and Lafleur 2003), the effect of the frequency will not be further discussed. The same applies for the polarisation as Antonova et al. (2016) and others have successfully used HH polarisation. Additionally, interacting and/or overlaying effects cannot be disentangled within the scope of this study and are therefore subject to further research.

VI. CONCLUSIONS

In this project, we assessed the feasibility of the detection of grounded ice with Sentinel-1 data. The signature of grounded ice could not be detected with the applied methodology. We identified the following points to be potential causes for the absence of the expected signature:

- The lakedepth in the study area has been underestimated. Grounded ice is only existent in the shallow border regions of the lakes which was obscured by the low resolution.
- Grounded ice is present in the studied area. Our approach is not suitable for the detection of the signature due to the discussed factors.

The former cause does not allow a statement about the general feasibility of our approach. The latter cause, however, raises concern about the suitability of Sentinel-1 data for the detection of grounded ice. Furthermore, this study emphasizes the importance of in-field measurements, particularly for methodologies that have not yet been proven to be robust.

Further research should continue to explore the feasibility of detecting grounded ice with Sentinel-1. Ideally this could be done in combination with in-field measurements to assess the influence of discussed factors in-depth. Another tool that could provide insightful auxiliary information for this approach is interferometry, as shown by Antonova et al. (2016).

ACKNOWLEDGMENT

We would like to express our appreciation to our lecturers Dr. Rogier De Jong, Dr. David Small and Adrian Schubert who have provided us with helpful information and material. They have always created a supportive and encouraging environment during the process of our project. Furthermore, our thank goes to Dr. Gabriela Schaepman-Strub who has helped us to estimate the prevailing circumstances of the study site by giving us an insight in her experience gained in the area.

References

Antonova, S., Duguay, C., Kääb, A., Heim, B., Westermann, S., Langer, M., & Boike, J. (2016). Monitoring bedfast ice in lakes of the lena river delta using terrasar-x backscatter and coherence time series..

Atwood, D. K., Gunn, G. E., Roussi, C., Wu, J., Duguay, C., & Sarabandi, K. (2015). Microwave backscatter from arctic lake ice and polarimetric implications. *IEEE Transactions on Geoscience and Remote Sensing*, *53*(11), 5972–5982.

Bartsch, A., Pointner, G., Leibman, M. O., Dvornikov, Y. A., Khomutov, A. V., & Trofaier, A. M. (2017). Circumpolar mapping of ground-fast lake ice. *Frontiers in Earth Science*, *5*, 12.

Boike, J., Georgi, C., Kirilin, G., Muster, S., Abramova, K., Fedorova, I., … Langer, M. (2015). Thermal processes of thermokarst lakes in the continuous permafrost zone of northern siberia–observations and modeling (lena river delta, siberia). *Biogeosciences*, *12*(20), 5941.

Duguay, C., & Lafleur, P. (2003). Determining depth and ice thickness of shallow sub-arctic lakes using spaceborne optical and sar data. *International Journal of Remote Sensing*, *24*(3), 475–489.

Engram, M., Arp, C. D., Jones, B. M., Ajadi, O. A., & Meyer, F. J. (2018). Analyzing floating and bedfast lake ice regimes across arctic alaska using 25 years of spaceborne sar imagery. *Remote Sensing of Environment*, *209*, 660–676.

Grosse, G., Jones, B., & Arp, C. (2013). Thermokarst lakes, drainage, and drained basins. *Treatise on Geomorphology, Volume 8*.

Jeffries, M. O., Wakabayashi, H., & Weeks, W. (1993). Ers-1 sar backscatter changes associated with ice growing on shallow lakes in arctic alaska. In *Geoscience and remote sensing symposium, 1993. igarss'93. better understanding of earth environment., international* (pp. 2001–2004).

Kabiri, K. (2017). Accuracy assessment of near-shore bathymetry information retrieved from landsat-8 imagery. *Earth Science Informatics*, *10*(2), 235–245.

Muster, S., Roth, K., Langer, M., Lange, S., Aleina, F. C., Bartsch, A., … others (2017). Perl: A circumarctic permafrost region pond and lake database. *Earth System Science Data*, *9*(1), 317.

Wakabayashi, H., & Nishito, Y. (2015). Monitoring of tundra lakes with c-band and l-band sar data. In *Geoscience and remote sensing symposium (igarss), 2015 ieee international* (pp. 2076–2079).

Wakabayashi, H., Weeks, W., & Jeffries, M. O. (1993). A c-band backscatter model for lake ice in alaska. In *Geoscience and remote sensing symposium, 1993. igarss'93. better understanding of earth environment., international* (pp. 1264–1266).

Xu, H. (2006). Modification of normalised difference water index (ndwi) to enhance open water features in remotely sensed imagery. *International Journal of Remote Sensing*, *27*(14), 3025-3033.

Zimov, S. A., Voropaev, Y. V., Semiletov, I., Davidov, S., Prosiannikov, S., Chapin, F., … Tyler, S. (1997). North siberian lakes: a methane source fueled by pleistocene carbon. *Science*, *277*(5327), 800–802.

Acknowledgements

First, I would like to sincerely thank my supervisor Dr. David Small, for supporting my idea for this thesis. As I was going through a difficult time, his very involved and continuous guidance was invaluable to me. I also want to thank Prof. Dr. Michael Schaepman for having given me the opportunity to carry out this research and Prof. Dr. Alexander Damm for pitching in after Schaepman's departure from the faculty. Furthermore, I also want to thank my parents, colleagues, friends and everyone who was involved in proofreading or otherwise supported me.

Personal Declaration

I hereby declare that the submitted thesis is the result of my own, independent work. All external sources are explicitly acknowledged in the thesis.

Date
January 29, 2021

Signature
Emanuel Vogel Emanuel Vogel